The diode-pumped continuous-wave Raman laser : classical, Quantum, and thermo-optic fundamentals
by Peter Aaron Roos

A thesis submitted in partial fulfillment of the requirements of the degree Masters of Science
Montana State University

Abstract:
This thesis describes the creation and development of far-off-resonance diode-pumped cw Raman lasers using high-finesse cavity enhancement from both theoretical and experimental standpoints. Comprehensive theoretical models are developed for the cw Raman system in the classical and quantum mechanical domains. The classical treatments include two separate derivations of the time-dependent cw Raman equations (one as an appendix), derivations of the analytical steady-state threshold power, impedance-matching power, all emitted powers, and conversion efficiency, as well as the system optimization with respect to every parameter available, and a useful frequency tuning picture (as an appendix). An entire chapter is devoted to the classical treatment of thermo-optic effects in this laser system including mode pulling and thermal lensing.

The quantum mechanical treatment uses the Heisenberg/Langevin approach to derive the Stokes output noise spectra analytically for this system. Subsequent analysis reveals the possibility of approaching perfect photon statistics transfer from the pump to the Stokes and generating nonclassical photon number statistics. An interesting and useful connection to the nondegenerate optical parametric oscillator is uncovered. The quantum mechanical approach is also used to show that a similar system can generate efficient cw anti-Stokes emission.

The process of constructing these laser systems and the subsequent measured behavior comprise the experimental component of this thesis. Diode laser frequency locking for this system is treated thoroughly as an exercise in precision frequency stabilization and control theory. The optimal designs of the diode laser pump source, the high-finesse Raman laser cavity, and the electronic servo are discussed. The use of injection locking and passive optical frequency stabilization are also addressed.

Using these construction and locking techniques, the results from diode-pumped cw Raman laser experiments in diatomic hydrogen gas are provided and are shown to compare favorably with the theoretical predictions. The results include steady-state data obtained from the first diode-pumped cw Raman laser, the first high efficiency cw Raman laser, a cw Raman laser pumped by an injection-locked diode laser, and the first cw Raman ring laser. Data confirming the effects of thermal mode pulling and lensing are also provided.

THE DIODE-PUMPED CONTINUOUS-WAVE RAMAN LASER: CLASSICAL, QUANTUM, AND THERMO-OPTIC FUNDIMENTALS

by

Peter Aaron Roos

A thesis submitted in partial fulfillment

of the requirements of the degree

Masters of Science

MONTANA STATE UNIVERSITY

Bozeman, Montana

October 2002

APPROVAL

of a dissertation submitted by

Peter Aaron Roos

This dissertation has been read by each member of the dissertation committee and has been found to be satisfactory regarding content, English usage, format, citations, bibliographic style, and consistency, and is ready for submission to the College of Graduate Studies

John L. Carlsten _____ 10-14-02
(Signature) Date

Approved for the Department of Physics

John C. Hermanson _____ 10-14-02
(Signature) Date

Approved for the College of Graduate Studies

Bruce R. McLeod _____ 10-16-02
(Signature) Date

STATEMENT OF PERMISSION TO USE

In presenting this dissertation in partial fulfillment of the requirements for a doctoral degree at Montana State University, I agree that the Library shall make it available to borrowers under rules of the Library. I further agree that copying of this dissertation is allowable only for scholarly purposes, consistent with "fair use" as prescribed in the U. S. Copyright Law. Requests for extensive copying or reproduction of this dissertation should be referred to Bell & Howell Information and Learning, 300 North Zeeb Road, Ann Arbor, Michigan 48106, to whom I have granted "the exclusive right to reproduce and distribute my dissertation in and from microform along with the non-exclusive right to reproduce and distribute my abstract in any format in whole or in part."

Signature 

Date 10/14/02

ACKNOWLEDGEMENTS

I must first thank my partner, Jennifer, my sister, Bonnie, and my parents, Kathy and Roger for their unwavering love and encouragement throughout my graduate work and especially while I was writing this thesis. They have been incredibly supportive during one of the most difficult, but rewarding times of my life.

I also thank Sally O'Neill for her critical guidance and assistance during the Fulbright application process. As a direct result of her efforts, I can also thank Tim Ralph, Andrew White, Rodney Polkinghorne, Michael Nielsen, Joe Altepeter, and all the folks at the University of Queensland physics for helping to make my experience in Australia one of the best of my life. This experience (the guidance of Tim and Andrew in particular) also led to the findings presented in Chapter 3.

I am grateful to Norm in the shop for teaching me basically everything I know about machining, as well as Margaret, Jeannie, Rose and Jeremy in the office for their assistance with my day-to-day activities. These people have kept me and the whole department running smoothly.

Thanks to Tom and Pete for their friendship and advice with frequency locking. These are two very talented physicists who have thankfully not lost their appreciation nor their devotion to the wonderful outdoors.

Thanks go to Sytil, Tina, Brian, and Jennifer for making the past year so enjoyable in the lab. Our lunchtime discussions will be sorely missed. Furthermore, Sytil was kind enough to edit this entire thesis. But more importantly, she played a significant role in the findings of Chapter 5. I had a wonderful time working with her this summer.

I thank Monty for his friendship and for keeping me sane with daily climbing or bouldering excursions. We shared many good times and laughs together. We've never discussed physics with each other, and I'm sure we never will. True lifelong dirtbag friends like Monty are impossible to replace.

I am also thankful to Randy for his friendship, climbing, and physics discussions during our graduate years. I greatly admire Randy's ability to balance his roles as a caring father and husband with his amazing skills and productivity as a physicist.

I give special thanks to my predecessor Jay not only for his true friendship, but also for giving me such an incredible head start in the field of cw Raman lasers. Jay has an extraordinary gift as an experimentalist in the lab. He is the most natural person in that environment that I've ever seen. I can only hope that some of his talent rubbed off on me. I'll always enjoy working with Jay in the lab, not to mention shooting pool and drinking beer with him at the bars. He's an all-round friend.

I am grateful to Josh Bienfang for some of the most stimulating physics discussions that I've had as a graduate student. Josh has an ability blend rock-solid mathematics and theory with superb experimental skills to yield unparalleled understandings of

physics. Of my contemporaries, he is the most talented all-round physicist that I know of (even though we have yet to actually meet in person). Josh played a *major* role in the development of Appendix B and Chapter 4. I've learned a great deal from our interactions and I truly hope they continue in the future.

I also thank Lei for his wonderful companionship and friendship during our graduate work. We shared both lab space and living space while writing our theses. During my year in Australia, I realized how valuable our day-to-day discussions on physics really were. Those interactions will be missed in the future. Almost every experiment in Chapter 6 was conducted with Lei. His dedication and attention to detail make him a superb physicist. His thoughtfulness and sense of humor make him an genuine friend.

Last, but definitely not least, I thank my advisor, John. This guy has undoubtedly had the single most profound influence on my development as a physicist. But the wonderful thing about John is that his teachings transcend physics. He has dramatically influenced my thoughts and philosophies about life as well. John magically combines knowledge, experience, skill, and compassion like no one I've ever met. He has provided guidance beyond anything I could have asked for. He will remain a cherished colleague and friend throughout my life.

TABLE OF CONTENTS

LIST OF TABLES

LIST OF FIGURES

ABSTRACT

This thesis describes the creation and development of far-off-resonance diode-pumped cw Raman lasers using high-finesse cavity enhancement from both theoretical and experimental standpoints. Comprehensive theoretical models are developed for the cw Raman system in the classical and quantum mechanical domains. The classical treatments include two separate derivations of the time-dependent cw Raman equations (one as an appendix), derivations of the analytical steady-state threshold power, impedance-matching power, all emitted powers, and conversion efficiency, as well as the system optimization with respect to every parameter available, and a useful frequency tuning picture (as an appendix). An entire chapter is devoted to the classical treatment of thermo-optic effects in this laser system including mode pulling and thermal lensing.

The quantum mechanical treatment uses the Heisenberg/Langevin approach to derive the Stokes output noise spectra analytically for this system. Subsequent analysis reveals the possibility of approaching perfect photon statistics transfer from the pump to the Stokes and generating nonclassical photon number statistics. An interesting and useful connection to the nondegenerate optical parametric oscillator is uncovered. The quantum mechanical approach is also used to show that a similar system can generate efficient cw anti-Stokes emission.

The process of constructing these laser systems and the subsequent measured behavior comprise the experimental component of this thesis. Diode laser frequency locking for this system is treated thoroughly as an exercise in precision frequency stabilization and control theory. The optimal designs of the diode laser pump source, the high-finesse Raman laser cavity, and the electronic servo are discussed. The use of injection locking and passive optical frequency stabilization are also addressed.

Using these construction and locking techniques, the results from diode-pumped cw Raman laser experiments in diatomic hydrogen gas are provided and are shown to compare favorably with the theoretical predictions. The results include steady-state data obtained from the first diode-pumped cw Raman laser, the first high efficiency cw Raman laser, a cw Raman laser pumped by an injection-locked diode laser, and the first cw Raman ring laser. Data confirming the effects of thermal mode pulling and lensing are also provided.

CHAPTER 1

INTRODUCTION

Stimulated Raman Scattering: A Brief Review

The stimulated Raman effect was discovered in 1962 [1], shortly after the advent of the laser. One can view this two-photon process most simply as an exchange of "pump" photons for lower energy "Stokes" photons through a stimulated interaction with a Raman-active medium as illustrated in Fig. 1. The energy difference between the incident pump and stimulated Stokes photons resides within the Raman medium after the interaction, often in the form of a molecular vibration.

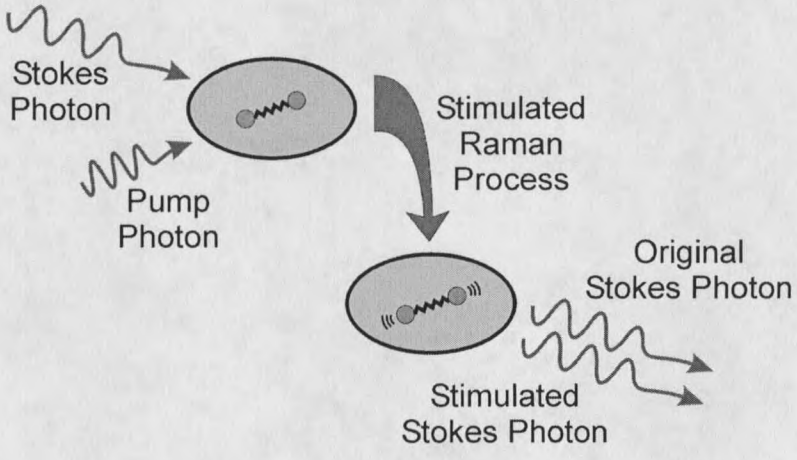

Figure 1. Simple picture of the stimulated Raman process. An incident pump photon is converted to a lower energy (longer wavelength) stimulated Stokes photon and the leftover energy remains in the Raman medium.

This process can result in exponential growth (amplification) of input Stokes light at the expense of the input pump light. But even when there is no input Stokes, the process can be initiated by spontaneous emission alone. In other words, by simply directing an intense pump laser through a Raman medium, some of the pump light will be converted to the Stokes frequency, as shown in Fig. 2. Stimulated Raman scattering (SRS) therefore provides, among other things, a valuable method of down-shifting the frequency of laser light. However, this stimulated process differs from parametric conversion processes in that the phase of the generated Stokes light doesn't directly depend on that of the pump. Due to this phase-insensitive amplification, the system shown in Fig. 2 is often considered to be an optically-pumped laser; more specifically, a Raman laser.

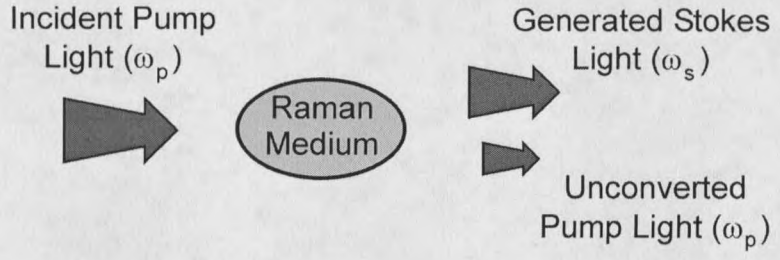

Figure 2. Frequency downconversion using the stimulated Raman process. Because this involves phase insensitive amplification of the Stokes light, the system shown is often called a Raman laser. The laser action is initiated by spontaneously emitted Stokes photons.

However, due to its third-order nonlinear nature, the stimulated Raman process requires substantial pump power to exceed the laser threshold and therefore to efficiently convert energy from the pump to the Stokes frequency. This obstacle is exacerbated by the fact that the frequency of the pump laser often does not match an atomic resonance of the Raman medium, as will be discussed. These two factors have traditionally relegated Raman conversion to the pulsed (as opposed to continuous-wave) laser regime where the required high peak powers can be achieved.

Given its importance in understanding the Raman process, a more detailed analysis of the Raman medium is now given. The nonlinear Raman medium, represented by ovals in Figs. 1 and 2, is often modeled quantum mechanically as a collection of three-level atoms or molecules, each in a lambda (Λ) configuration as depicted in Fig. 3. As the figure suggests, it is useful to juxtapose two different Raman transition regimes in order to place the focus of this thesis into perspective.

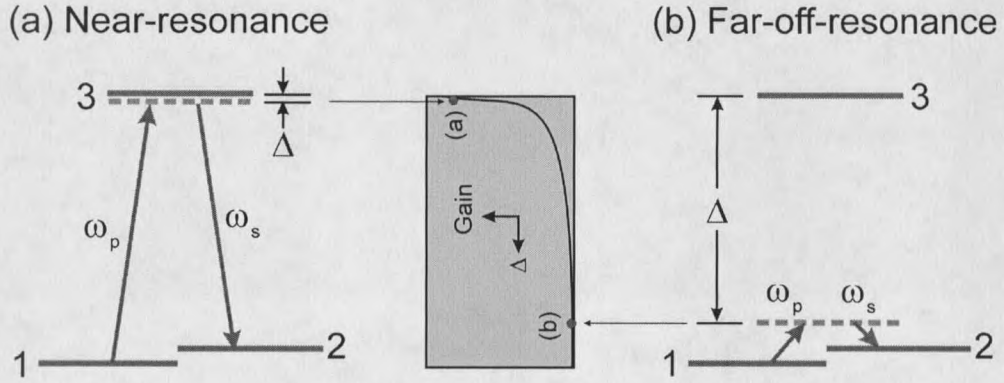

Figure 3. Simplified energy level diagrams for the (a) near-resonance and (b) far-off-resonance Raman processes. The large detuning (Δ) causes the gain for the far-off-resonance process to be much lower than for the near-resonance process.

Near-resonance SRS

Figure 3(a) shows the near-resonance case where both the pump and Stokes field frequencies nearly match the single-photon atomic transition frequencies (i.e. the single-photon detuning Δ is small). Gain for the Raman process is maximized in this near-resonance regime. Through the process shown, energy can be converted from the field at the pump frequency (ω_p) to the Stokes frequency (ω_s). Energy conservation requires that the atomic system be promoted to an excited state (level 2 in the figure) during the interaction. The quantum structure of the atom therefore determines the Raman frequency shift between the input pump and generated Stokes light.

By capitalizing on the enhanced gain in this near-resonance regime, cw Raman emission has been achieved experimentally in ammonia [2, 3], neon [4, 5, 6, 7], and atomic vapor [8, 9]. However, there are two significant drawbacks to operating in this regime. First, these systems depend critically on the pump laser's spectral proximity to the single-photon transition frequency. As evident from the schematic in the center of Fig. 3, small changes in the pump laser's frequency alter the gain significantly. This limitation substantially restricts the suitable pump sources as well as the spectral coverage and tunability of the Stokes output. Secondly, additional processes (other than Raman) based on the population of level 3 complicate the behavior of these systems both theoretically and experimentally when the single-photon detuning is small.

Far-off-resonance SRS

In sharp contrast to the near-resonance systems, Fig. 3(b) depicts the far-off-resonance Raman regime, where Δ is very large. This means that the field frequencies are not even remotely close to the single-photon atomic transition frequencies. Note, however, that the two-photon Raman transition is assumed resonant [$\omega_p - \omega_s = \omega_{21} = (E_2 - E_1)/\hbar$], as it was for the near-resonance case. The relative energy level spacings shown, including the virtual level (represented by a dashed line in the figure), are to-scale for the molecular system analyzed in this thesis (diatomic hydrogen gas). Again, energy is transferred from the pump to the Stokes frequency, with the difference remaining in the medium. But this time, as will be shown in later chapters, the extreme single-photon detuning isolates the Raman process from population-based effects. Furthermore, as can be seen from the center schematic in Fig. 3, tuning the pump laser frequency (which therefore tunes the Stokes output frequency) results in very little change in the Raman gain when Δ is this large. For hydrogen, this means that all visible and near infrared pump lasers will experience very similar gain and allows for the possibility of broadly tunable Stokes output. The primary drawback of this regime is the abysmal gain realized for such large single-photon detuning. In fact, esteemed Raman researcher and Nobel laureate Nicolaas Bloembergen stated in 1967: "The light intensity required to obtain an appreciable gain is so high that pulsed solid-state lasers are essential [10]."

Since that time, two techniques have led to the realization of cw Raman amplification and laser oscillation in the far-off-resonance regime. Both substantially increase the effective interaction length/time for Raman conversion in order to compensate for the reduced gain far from resonance. The first of these techniques involves the propagation of both the pump and the Stokes fields in Raman-active single-mode optical fiber [11, Chapter 8]. The glass core of the fiber itself serves as the Raman medium [12]. Due to the amorphous nature of glass, Raman gain occurs for vibrational transitions over a very broad spectral region with a peak at 13.2THz (440cm^{-1}). The process will likely play a significant role in telecommunications where multiple Raman shifts in optical fiber are used to convert existing cw lasers to wavelengths needed for telecommunications amplifiers [13]. However, in spite of the increased interaction length within the fiber, multi-watt pump lasers are typically required for these devices and cascaded Stokes shifts are often necessary to reach the target wavelength because a single shift is too small [14, 15, 16]. Furthermore, other nonlinear processes can compete with the Raman conversion [11].

The second technique currently used for far-off-resonance cw Raman conversion is that of high-finesse cavity enhancement. Instead of propagating long distances in a fiber, this method capitalizes on the prolonged photon storage time and the corresponding optical power enhancement within a high-finesse Fabry-Perot cavity [17, Chapter 11] to dramatically improve the effective interaction length for cw Raman conversion. This technique provides the foundation for the work presented in this

thesis and I'll therefore now narrow the focus of this introductory discussion accordingly.

Cavity-Enhanced CW Raman Lasers

Due to relatively recent improvements in mirror coating technology, Fabry-Perot optical cavities, or resonators, can now exhibit optical power enhancement factors exceeding 10^5 [18]. Furthermore, the high-finesse cavity (HFC) mirrors can be coated for two wavelengths, rather than just one. As a result, by enhancing both the pump and the Stokes fields within a HFC containing a gaseous Raman medium, the third-order nonlinear Raman transition can be enhanced by factors exceeding 10^9. This can reduce the typical far-off-resonance Raman laser threshold from hundreds of kilowatts to hundreds of microwatts. Figure 4 illustrates the benefit of double cavity enhancement by comparing the Raman laser threshold for three different cavity styles: a multi-pass cell, a HFC that is resonant just for the Stokes, and a HFC that is resonant for both the pump and the Stokes. As a result of the HFC enhancement at both wavelengths, the stimulated Raman laser threshold can be reached using low-power ($<$100mW) cw pump sources.

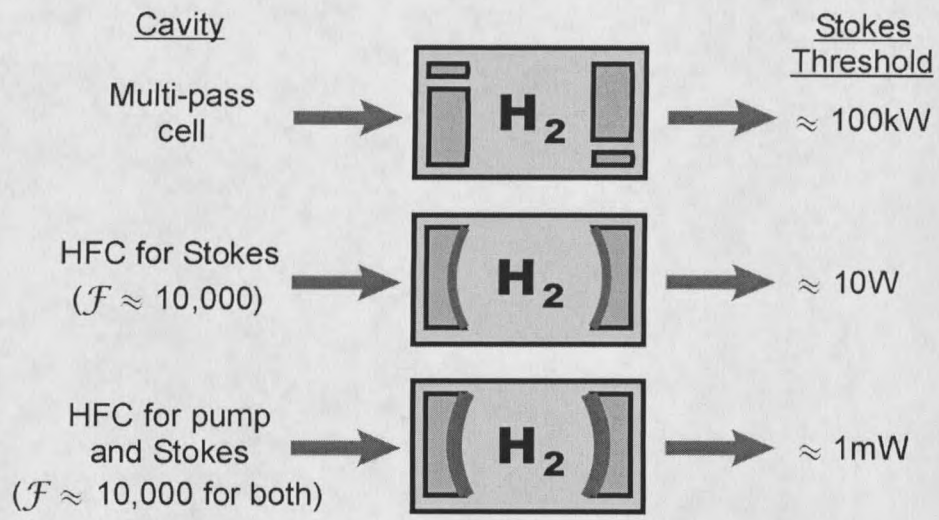

Figure 4. Diagram depicting the Stokes laser threshold for three different enhancement techniques. The diagram emphasizes the usefulness of high-finesse cavity (HFC) enhancement of both the pump and the Stokes fields. Specifically, the far-off-resonance Raman transition can be enhanced by nearly nine orders of magnitude.

However, this substantial cavity enhancement is not without cost. Because the cavity finesse is so high, its linewidth (or spectral bandpass) is necessarily very narrow. This means that if one wishes to build optical power within the HFC for Raman conversion, the pump laser's frequency/phase must be stabilized to that of a cavity resonance. Fortunately, precision laser stabilization techniques have received considerable attention in recent years in such fields as coherent communications [19, and references therein], atomic physics [20, and references therein], high-resolution spectroscopy [21, and references therein] and precision metrology [22, and references therein], in addition to other forms of nonlinear optical frequency conversion. In fact, HFCs (with no gas between the mirrors) are themselves often used as phase/frequency references to which lasers are stabilized [23, 24, 25].

It is therefore not surprising that the basic physical design for a cw Raman system is similar in concept to those of laser stabilization schemes as well as other cavity-enhanced nonlinear processes. As shown in Fig. 5, at its most basic level, the Raman laser setup can perhaps be viewed as containing three essential elements: The pump laser, the stabilization system, and the HFC. The pump laser provides the input energy for the process, the HFC containing hydrogen gas provides the conditions necessary for nonlinear conversion of the pump light into Stokes light, and the stabilization system ensures that the pump laser remains resonant with the HFC.

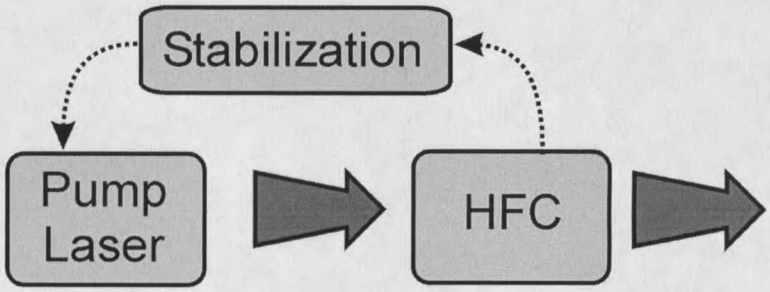

Figure 5. Simplified block diagram of the essential cw Raman laser elements. The high-finesse cavity (HFC) is filled with diatomic hydrogen gas.

Using these concepts, far-detuned cw Raman lasing was first achieved in 1998 using a stable, frequency-doubled Nd:YAG laser as the pump source at 532nm [26, 27]. The system generated several milliwatts of Stokes power at 683nm with a peak photon conversion efficiency of 27%. The output was characterized with respect to its time dependent behavior [27], continuous tuning [28], and linewidth [27]. This system also provided the first evidence of thermally-induced intensity dependent refractive

index [29] and coherent anti-Stokes generation [30]. But perhaps most importantly, it provided experimental confirmation of a Raman laser threshold below 1mW with measured cavity finesses near 13,000 for each of the two wavelengths. This pioneering work therefore confirmed the possibility of using diode lasers as pump sources.

Diode Pumping and Applications

Diode lasers are ideal pump sources for cavity-enhanced cw Raman lasers from an applications standpoint owing to their relative low cost, small physical size, broad spectral coverage, and tunability [20, 31]. It can be seen from Fig. 3 that if the input pump frequency is tunable, then the output Stokes frequency can tune as well (i.e. the virtual level will shift). In fact, Fig. 6 shows that by Raman shifting existing room temperature diode lasers in just two gases, gap-free spectral coverage from the visible past 5μm can be obtained. This diode laser frequency conversion technique becomes even more attractive when one considers the modest pump power requirements [32], high output power possibilities [33], high conversion efficiencies [34], as well as the exceptional spatial and spectral purity of the output [27]. The primary drawback of using diode lasers as pump sources is the limited single-mode output power currently available from commercial devices.

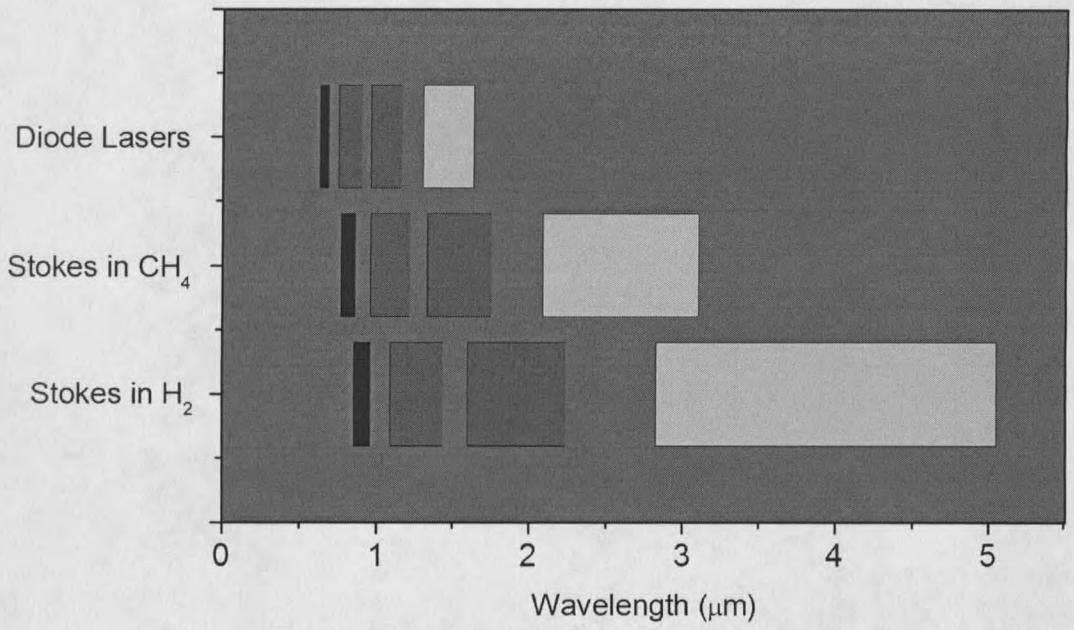

Figure 6. Diagram showing the spectral coverage of currently available room temperature diode lasers and their Raman-shifted outputs in methane and diatomic hydrogen gas. This figure was originally developed by John Carlsten.

Applications for relatively inexpensive, high quality, moderate power, near-infrared laser sources are widespread, yet there is currently a dearth of such sources in much of the spectral region. As a research tool, the GHz-range continuous frequency tuning and kHz-range linewidth of cw Raman lasers lend themselves well to the field of high resolution spectroscopy. In related fields, the possibility exists to create compact diode-pumped systems for remote sensing and on-site pollutant detection. Furthermore, frequency doubling the output of a Raman laser near 1178nm could generate a source for conducting atomic physics experiments and for adaptive optics using the sodium vapor transition near 589nm [35]. This would provide a relatively inexpensive alternative to the cumbersome cw dye laser which is predominantly used at this time.

In the field of precision metrology, cw Raman lasers may also provide a new method of frequency comb generation for laser stabilization [22]. Additional applications will undoubtedly also be found in other scientific fields and industries.

Clearly, the possibility exists for widespread use of cw Raman lasers. However, their niche will develop amongst higher power cw optical parametric oscillators, simpler diode pumped fiber lasers, less expensive communications wavelength diode lasers, as well as the cryogenically-cooled quantum cascade and lead salt lasers, just to name a few. The precise role that cw Raman lasers will play in the near-infrared arena remains to be seen.

Ring-Cavity Geometry

Most of the applications for cw Raman lasers rely on their long and short-term amplitude and frequency stabilities. Several factors, including stability, favor a ring-cavity geometry [17, pages 532–538] over a linear (two-mirror) geometry for cavity-enhanced cw Raman conversion. Examples of these two cavity geometries are shown schematically in Fig. 7. Furthermore, the traditional challenge of obtaining unidirectional output from a ring laser is elegantly averted in the Raman system, as discussed below.

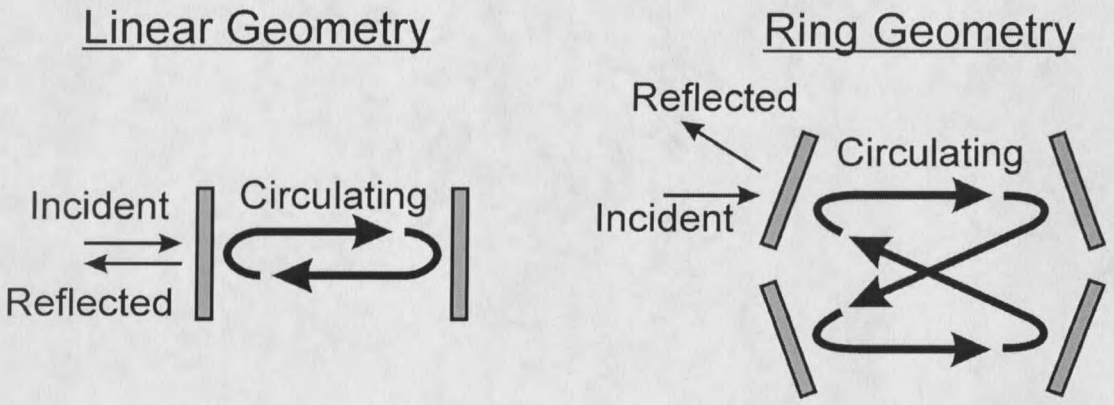

Figure 7. Diagram showing the incident, reflected, and circulating beams of a linear cavity and a bow-tie ring cavity. The reflected field does not return to the source for the ring geometry.

Perhaps the most important advantage of the ring cavity over its linear counterpart for diode-pumped Raman lasers is the elimination of optical feedback from the input mirror. For the linear cavity, the reflected-plus-transmitted pump field from the input mirror returns directly along the input path towards the pump laser, as shown in Fig. 7. Such optical feedback can seriously debilitate the stability of the pump source, particularly for diode lasers, [20, and references therein] and can cause severe locking instabilities. Substantial optical isolation of the pump laser is therefore a necessity with linear cavity setups. But even with 60-70 dB of isolation, the effects of optical feedback can still be observed. On the other hand, the reflected-plus-transmitted field does not return to the pump laser when a ring cavity is employed. This allows one to minimize or even omit the often-expensive optical isolators.

A second advantage of the ring laser geometry is the increased interaction volume within the Raman active medium. This dilutes the deleterious effects of heat

generation [29, 36] and also offers additional gain with each pass. In contrast to most applications, it is not necessary to focus tightly since the gaseous gain medium fills the entire intracavity region. Additionally, even though it has not been an issue for the linear cavity Raman lasers, the traveling wave nature of the circulating field in the ring cavity also prohibits standing wave effects such as spatial hole burning [17, pages 316–323]. This is an enormous advantage for other ring-cavity laser systems.

Perhaps the most intriguing aspect of the ring-cavity Raman laser is its inherent unidirectional operation. In typical ring lasers, symmetry in the gain between the forward and backward directions can cause non-stable, bi-stable, or dual-mode operation. [17, pages 534–535] Intracavity optical elements are therefore often required to coerce the laser to oscillate stably in a single direction. However, due to preferential Doppler broadening of the Raman transition in the backward direction, the ring-cavity cw Raman laser exhibits inherent stability in the forward direction when tuned to the Raman transition line-center.

The drawbacks of using a ring cavity for Raman conversion include the added complexity in design, the cost of additional mirrors, and a slightly lower cavity finesse. As will be shown in Chapter 2, any transmission through the extra mirrors enters as a loss in the Raman equations, and will therefore degrade the conversion efficiency from pump to Stokes power. However, with high-quality and properly chosen mirrors, this drawback is insignificant.

Overview of this Thesis

This thesis describes the classical, quantum, and thermo-optic fundamentals of the diode-pumped cw Raman laser from both theoretical and experimental standpoints. It is intended as an educational tool rather than a reproduction and collection of publications. I attempt throughout to either describe each conceptual jump in detail through the extensive use of appendices, or to refer the reader explicitly to adequate resources. In light of this, the reader who finds the material overly explanatory can alternatively find the essential results and information in the pertinent journal publications.

The remainder of the thesis can be partitioned into two segments. The theoretical segment includes classical, quantum, and thermo-optic treatments of the cw Raman laser system. The experimental segment describes the construction, operation, and measured results of diode-pumped cw Raman lasers.

The classical treatment in Chapter 2 is used to derive analytical equations to describe the basic cw Raman processes. I make a concerted effort to retain as much simplicity and clarity as possible in this treatment. The chapter focuses on the ring-geometry Raman laser cavity, but the methods can be applied equally well to the linear cavity. In fact, a comparison is made between the two cavity styles as part of Appendix B. Also included in the classical analysis is a mathematically and practically oriented discussion of the optimal construction and operation parameters

for the Raman system.

The quantum optical treatment provided in Chapter 3 is used to derive the time dependent operator equations for the cw Raman laser in the Heisenberg picture starting from the system Hamiltonian. The Heisenberg picture facilitates physical understanding of the system. As a result, interesting connections are drawn between the cw Raman laser and the nondegenerate optical parametric oscillator as well as the traditional (population-based) laser. The quantum optical treatment also predicts the possibility of nonclassical behavior from the cw Raman system and generates analytical expressions for the output intensity noise (which include quantum noise).

Important thermo-optic effects are addressed theoretically in Chapter 4. The treatment deals with both the thermally-induced mode pulling and the thermal lensing that occur within the Raman laser cavity as functions of the generated Stokes power. The resulting modifications to the basic cw Raman laser equations are derived and discussed. The thermo-optic effects present the largest fundamental obstacle to be overcome in creating stable, high-power cw Raman systems.

Chapter 5 focuses on the frequency stabilization of the diode pump source to the HFC for Raman conversion. This is perhaps the most important and challenging experimental task involved in the construction of these systems. Both passive and active stabilization techniques are discussed, but a detailed description of only the active electronic locking procedure is given. Specific descriptions of the external-cavity pump laser, the high-finesse Raman laser cavity, and the high-bandwidth locking servo

are given. The chapter also describes the implementation of the injection locking technique to enhance the often-meager power of the external-cavity diode laser pump source.

Some experimental results that have been measured when the pump laser is stabilized to the high-finesse Raman laser cavity are provided in Chapter 6. Specifically, the chapter documents the first diode-pumped cw Raman laser, the first high-efficiency Raman laser, the implementation of injection locking in the Raman laser system, the thermal mode pulling and lensing, and the unidirectional operation of the first cw Raman ring laser. All of the experimental results are compared to the theoretical models developed in Chapters 2-4. The final chapter is used to review the primary achievements and findings presented in this thesis and to discuss possible future research directions.

CHAPTER 2

CLASSICAL THEORY

The goal of this chapter is to provide the most straightforward time-dependent theoretical description of the far-off-resonance cw Raman laser possible. I therefore strongly favor simplicity at the expense of rigor. Although many subtleties are lost in the process and are left to be discovered in later chapters, it is my hope that the results presented here allow insight into the basic physical processes that are involved in cw Raman lasers. When appropriate, I try to mention the shortcomings or limitations of the results. I also use four appendices to cover some important topics in more depth. In particular, Appendix B is used to derive the Raman laser equations from first principles using the Lamb approach. Consequently, some may find this appendix more useful than the cursory treatment given in the main chapter. I find myself referring back to this appendix perhaps more than any other part of the thesis. Also of particular interest is Appendix D, which documents the development of a useful physical tuning picture for the cw Raman system.

The treatment in this chapter is purely classical. Here, the quantum structure of the atom is conveniently avoided by connecting the Raman gain to an empirically-based parameter (the plane-wave gain coefficient). Indeed, this is how the Raman gain is typically obtained in practice when theory is compared to experiment. Also

note that an adequate physical description of the Raman gain can be established using strictly classical considerations [37]. The chapter following this provides the opposite extreme where both the fields and the atoms are treated quantum mechanically.

This chapter begins with a review of previous theoretical studies of cw Raman systems. In the second section, rate equations for both the pump and the Stokes intracavity optical powers are derived. Along the way, the gain constant for the Raman medium in the focused geometry is obtained simply by connecting to the results of existing pulsed Raman laser work. In the third section the steady-state limits of the intracavity Raman power equations are taken in order to generate the laser threshold condition. Equations describing the output versus input powers in the steady state also follow directly from the intracavity powers. The fourth section combines mathematical with practical considerations in determining the optimum construction and operation parameters for cw Raman systems. The last section consolidates the findings of the chapter and connects with the material to follow.

The appendices that are associated with this chapter are as follows: Appendix A provides a simple method of obtaining a very useful general laser cavity field equation. The equation can be applied to both the pump and the Stokes fields for the system at hand. Appendix B provides a rigorous derivation of the Raman laser equations in the focused geometry starting from the Maxwell equations. This appendix can be viewed as an alternative to the treatment given in the main chapter. Appendix C shows that the fundamental eigenmode of a single pass through the bow-tie ring cavity

can be approximated by that of a linear cavity when the reflection angles are small. Appendix D provides a very useful physical picture of the frequency tuning behavior for the cw Raman laser. Throughout the chapter and the appendices, I attempt to follow Siegman's notation in *Lasers* as closely as possible [17].

Previous Work

The origins of cw Raman laser theory can be traced to the mid-1960's where amplifier theory (based in the spatial domain rather than the time domain) was the dominant approach [38, 39]. Most of this early work was devoted to predicting and optimizing the laser threshold in the plane-wave limit, but subsequent treatments incorporated beam focusing. In particular, Boyd and coworkers developed very useful analytic relations between the often-measured plane-wave gain coefficient and the Raman gain in the focused geometry [40].

The experimental realization of far-off-resonance cw Raman lasing in 1998 was followed by several theoretical treatments. Repasky and coworkers developed a steady-state interferometric model, predicting a peak photon conversion efficiency of 50% for symmetric mirrors (meaning the front and back mirrors have identical reflectivities) and 100% for asymmetric mirrors (meaning the front and back mirrors have different reflectivities) [41, 42]. The researchers discovered that the peak conversion efficiency occurs at a pump rate of four times the threshold value. Peterson and coworkers used an amplifier theory approach in another steady-state treatment [43]. They showed

that under certain circumstances, a reduction in the mirror reflectivities could lead to greater power extraction, thereby reinforcing the findings of Repasky *et al.* Brasseur and coworkers developed the first time-dependent cw Raman laser theory [44] based on a general laser derivation that was introduced by Lamb long ago [45]. In the appropriate limits, all the treatments mentioned above can be shown to generate equivalent results in the steady state (aside from a factor of two error in the Repasky treatments). Quantum optical treatments that are related to cw Raman lasers are discussed in the next chapter.

Raman Power Rate Equations

Starting from the general laser cavity field equation derived in Appendix A, this section derives time-dependent equations for both the pump and Stokes optical powers. The Raman gain is obtained by connecting to previous pulsed Raman work.

The treatment given here is based upon the bow-tie ring cavity depicted in Fig. 8, but it can be applied equally well to the linear cavity geometry as discussed at the end of Appendix B. In the figure, the E's represent one-way traveling wave electric field amplitudes, while the r's represent amplitude reflectivities. The cavity is assumed to exhibit a high finesse so that all the reflectivities are very nearly unity. The mirror with reflectivity r_0 serves as both the input (for the pump) and output (for the Stokes) coupler. The other three mirrors exhibit identical reflectivities (r_1). It will be shown that r_1 should be chosen as high as possible. All the mirrors have equal curvature so

that a focus occurs midway between each pair and there exists a symmetry axis about the center of the cavity in both the horizontal and vertical dimensions as can be seen in Fig. 8. The gain medium occupies the entire intracavity volume. The beam path within the cavity is composed of four passes; two short passes of length L (horizontal in the figure), and two long passes of length $L' = L/\cos(2\theta)$ (diagonal in the figure). In this work, the angle θ is small so that $L \approx L'$.

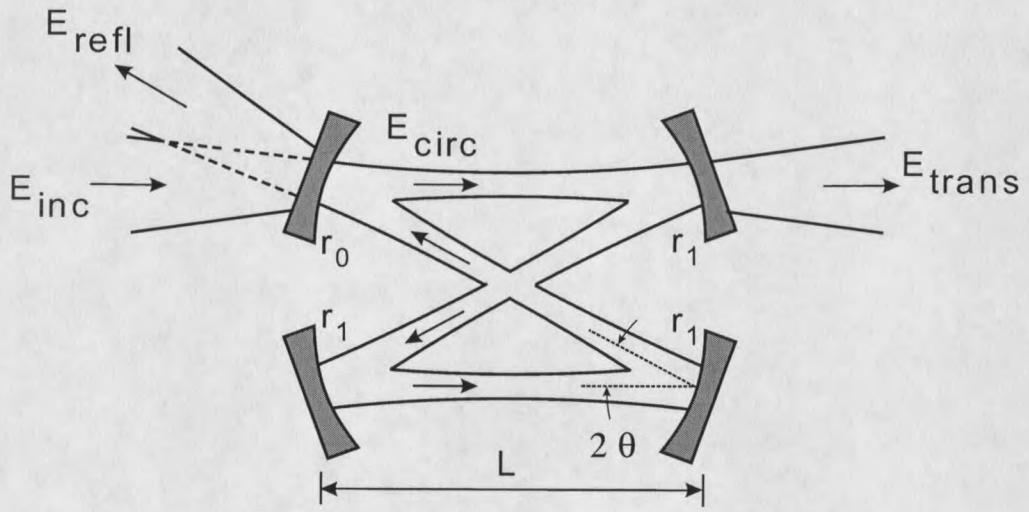

Figure 8. Illustration showing the ring-cavity geometry with the relevant fields. The laser medium occupies the entire intracavity volume.

From Eq. (A.5) in Appendix A, the amplitudes of both the pump and the Stokes fields within the laser cavity obey the equation

$$\frac{dE(t)}{dt} = -\frac{\gamma}{2}E(t) + c\,\alpha_m E(t) + \tau_{\mathrm{rt}}^{-1}\sqrt{T_0}E_{\mathrm{inc}}(t), \tag{2.1}$$

where $E(t)$ represents the real one-way circulating field amplitude (the subscript "circ" has been dropped from the notation used in Appendix A), $E_{\mathrm{inc}}(t)$ is the incident

field amplitude (also real), c is the speed of light, $\tau_{\rm rt} = p/c$ is the round-trip time in the cavity, $p \approx 4L$ is the round-trip cavity length, α_m is Siegman's gain (or loss) coefficient that is due to interaction with the atomic medium [17, page 272], T_0 is the power transmissivity of the input coupler[1], and

$$\gamma \equiv \tau_{\rm rt}^{-1}\,(1 - R_{\rm rt}) \tag{2.2}$$

is the cold-cavity power decay rate, where $R_{\rm rt} = R_0 R_1^3$ is the round-trip power reflectivity for the ring cavity ($R_{\rm rt} \equiv r_{\rm rt}^2$). Eq. (2.1) simply indicates that three factors can affect the circulating field dynamics. Specifically, the first term on the right represents decay due to transmission and absorption of the mirrors (loss), the second term represents the effect of the intracavity medium (loss or gain), and last term is due to an external input field (gain).

Because the optical power is proportional to the field magnitude squared ($P = const. \times E^2$ for real E) differentiation of this power leads to the equation

$$\frac{dP(t)}{dt} = const. \times 2E(t)\frac{dE(t)}{dt}. \tag{2.3}$$

Using this expression, Eq. (2.1) can be converted to a power rate equation to yield

$$\frac{dP(t)}{dt} = -\gamma P(t) + 2c\,\alpha_m P(t) + 2\tau_{\rm rt}^{-1}\sqrt{T_0}\sqrt{P(t)}\sqrt{P_{\rm inc}(t)}. \tag{2.4}$$

This expression is also quite general and applies to a wide variety of laser systems. All the parameters in the equation can be directly measured with the possible exception

[1] The variable T_0 used here for the input coupler transmissivity is also used for temperature in Chapter 4.

of the laser gain coefficient, α_m. Attention will now be focused on this parameter for the specific Raman gain medium at hand.

Raman Gain Coefficient

This subsection is devoted to relating Siegman's laser gain coefficient, α_m (units 1/m), in Eq. (2.4) to the commonly-measured Raman plane-wave gain coefficient, denoted as α (units m/W). This is accomplished somewhat superficially by simply connecting to previous Raman research in the pulsed laser regime. A more thorough treatment of the laser gain beginning with the Maxwell equations is given in Appendix B, but the results are identical. That appendix also compares the results to that of a standing-wave cavity.

Boyd and coworkers contributed substantially to the field of nonlinear optics through (among other things) their analyses of parametric and stimulated interactions in the focused geometry [40, 46]. Of primary interest here is their expression for the fractional increment in Stokes power per pass given by Eq. (3.8) of Ref. [40]. For the case when the confocal parameters for the two wavelengths are the same (this is true when a single cavity is used to resonate both wavelengths), Rabinowitz and coworkers simplified Boyd's expression to [47]

$$\frac{\Delta P_s}{P_s} = \frac{4\alpha P_p}{\lambda_p + \lambda_s} \tan^{-1}(L/b), \qquad \text{(single pass, traveling wave)} \qquad (2.5)$$

where the pump and Stokes are distinguished by the subscripts p and s, respectively, the circulating pump power P_p is assumed to be constant over a single pass, α is the

plane-wave gain coefficient (*not* Siegman's gain coefficient), λ's are wavelengths, b is the confocal parameter, and L is the length of one focused pass in the cavity (*not* the round-trip length).

There are several obstacles presented with applying Eq. (2.5) to the ring cavity. First off, due to the non-zero reflection angle from each mirror, the stable fundamental resonator mode exhibits elliptical beam profiles at the four waists. As a result, the confocal parameters for the two radial dimensions are not the same. Second, the lengths and confocal parameters for the short passes are different from those of the long passes. However, Appendix C shows that when the reflection angle is small, one can assume that each of the four passes in the bow-tie cavity is effectively identical to that of a linear cavity, but with a traveling- rather than a standing-wave axial dependence.

To connect Eq. (2.5) with the power rate equation derived above, one can consider just the medium gain term in Eq. (2.4) for the moment (the second term on the right). When the terms involving the mirrors are ignored, the resulting differential equation is separable and can be written

$$\frac{dP_s(t)}{P_s(t)} = 2c\,\alpha_{m,s}\,dt. \tag{2.6}$$

This equation can be directly integrated over the round-trip time ($\tau_{rt} = p/c$). The integration is particularly easy when one notes that $P_s(t)$ can be assumed nearly

constant over the round-trip time. The result can then be written

$$\frac{\Delta P_s}{P_s} = 2p\,\alpha_{m,s}, \qquad \text{(round trip)} \tag{2.7}$$

where $\Delta P_s \equiv P_s(\tau_{rt}) - P_s(0)$. Note that this last step is incompatible with systems for which the single-pass gain is significant. The total fractional change in Stokes power given by Eq. (2.7) is just the sum of the contributions from each of the four single passes from Eq. (2.5). That is, when the angle θ is small (See Fig. 8), the four passes yield a total fractional Stokes power change of

$$\frac{\Delta P_s}{P_s} = 4 \times \frac{4\alpha P_p}{\lambda_p + \lambda_s} \tan^{-1}(L/b). \qquad \text{(round trip, traveling wave)} \tag{2.8}$$

Equating Eqs. (2.7) and (2.8), and solving for Siegman's gain coefficient for the Stokes gives

$$\alpha_{m,s} = \frac{P_p}{2pP_1}, \tag{2.9}$$

where the constant

$$P_1 \equiv \frac{\lambda_p + \lambda_s}{16\,\alpha \tan^{-1}(L/b)} \qquad \text{(bow-tie cavity unity gain constant)} \tag{2.10}$$

has units of power and can be interpreted as the circulating pump power required to achieve unity gain over a distance of one round trip. As indicated in Appendix C, P_1 can be modified to accommodate larger reflection angles in the bow-tie cavity.

To obtain an expression analogous to Eq. (2.9) for the pump gain coefficient, one can notice that energy conservation requires the power gained by the Stokes per pass

to be related to the power lost by the pump through

$$\Delta P_p = -\frac{\lambda_s}{\lambda_p}\Delta P_s. \tag{2.11}$$

With this, and using expression (2.7) as well as an identical equation for $\Delta P_p/P_p$, one can quickly identify the pump gain coefficient as

$$\alpha_{m,p} = -\frac{\lambda_s}{\lambda_p}\frac{P_s}{2p\,P_1}. \tag{2.12}$$

With the gain constants given by Eqs. (2.9) and (2.12), Eq. (2.4) can now be used to generate the time-dependent equations for the pump and Stokes circulating powers

$$\frac{dP_p}{dt} = -\gamma_p P_p - \frac{\lambda_s}{\lambda_p}\tau_{\mathrm{rt}}^{-1}\frac{P_s P_p}{P_1} + 2\tau_{\mathrm{rt}}^{-1}\sqrt{T_{p,0}}\sqrt{P_p}\sqrt{P_{\mathrm{inc}}} \tag{2.13}$$

$$\frac{dP_s}{dt} = -\gamma_s P_s + \tau_{\mathrm{rt}}^{-1}\frac{P_s P_p}{P_1}. \tag{2.14}$$

The explicit time dependence was omitted here for simplicity and it was assumed that no incident Stokes beam exists (no "seed"). These two equations are the primary results of this section. They give the dynamic behavior of the circulating powers in the two active cavity modes. All coefficients are given in terms of measurable or tabulated quantities. To find the laser system's intensity noise, the equations can be solved numerically or they can be linearized about the steady-state values and solved analytically. Such a treatment will be postponed until the next chapter so that quantum noise can be included.

Steady-State Powers

The steady-state limit of Eqs. (2.13) and (2.14) can be taken by setting the time

derivatives to zero. In this limit, and using Eq. (2.2), the circulating pump and Stokes powers above threshold become

$$P_p = P_1(1 - R_{s,\mathrm{rt}}), \tag{2.15}$$

$$P_s = \frac{\lambda_p}{\lambda_s}\left[\left(\frac{4\,T_{p,0}\,P_1 P_{\mathrm{inc}}}{1 - R_{s,\mathrm{rt}}}\right)^{1/2} - P_1(1 - R_{p,\mathrm{rt}})\right]. \tag{2.16}$$

It should be noted that a second set of solutions is also possible from Eqs. (2.13) and (2.14). The second set corresponds to zero Stokes power generation and represents stable solutions only below threshold.

Note that the circulating pump power given by Eq. (2.15) is clamped (independent of incident power) above threshold. The system therefore acts as an optical power limiter for the incident pump light. As discussed in Chapter 3, similar clamping behavior is also observed in both the nondegenerate optical parametric oscillator and the traditional (population-based) laser. Also, the intracavity Stokes power is predicted to grow as the square root of the incident pump power. However, it should be mentioned here that the intracavity pump power ceases to clamp and the Stokes power departs from a strictly square-root dependence on the incident pump power when significant Stokes power is generated (typically $\gtrsim$10mW for the ring cavity). These effects and the associated modifications to Eqs. (2.15) and (2.16) are due to thermal lensing within the laser cavity and are discussed at length in Chapter ??.

Threshold Power

The incident pump power necessary to reach the Stokes laser oscillation threshold

can be obtained by setting Eq. (2.16) to zero. This yields

$$P_{\rm th} = \frac{P_1}{4}\frac{(1-R_{p,\rm rt})^2}{T_{p,0}}(1-R_{s,\rm rt}) \tag{2.17}$$

$$\approx \pi^2 \frac{P_1}{\mathcal{F}_p\,\mathcal{F}_s}, \qquad (T_{p,0} \approx 1 - R_{p,\rm rt}), \tag{2.18}$$

where the approximate equality holds when the input coupler transmissivity dominates the other cavity losses for the pump. The symbols $\mathcal{F}_p$ and $\mathcal{F}_s$ are the cold-cavity (i.e. no intracavity medium) finesses of the resonator at the pump and the Stokes wavelengths, respectively. They are of the form [17, page 436]

$$\mathcal{F} \equiv \frac{\pi\sqrt{r_{\rm rt}}}{1-r_{\rm rt}}$$

$$\approx \frac{2\pi}{1-R_{\rm rt}}. \tag{2.19}$$

Approximation (2.18) highlights the usefulness of enhancing both the pump and Stokes fields in the cavity since the threshold pump power scales inversely with the *product* of the two finesses.

Emitted Powers

The optical powers outside the cavity can be easily obtained by multiplying Eqs. (2.15) and (2.16) by the appropriate power transmission coefficients, with the exception of the pump power reflected from the input coupler. In this case, the total reflected field is a coherent sum of the the transmitted portion of the circulating pump field and the (out of phase) reflected portion of the incident field

$$E_{\rm refl} = t_{p,0}\,E_p - r_{p,0}\,E_{\rm inc}. \tag{2.20}$$

Converting this equation to optical power yields

$$P_{\text{refl}} = \left(\sqrt{T_{p,0}P_p} - \sqrt{R_{p,0}P_{\text{inc}}}\right)^2. \tag{2.21}$$

Using this result and Eqs. (2.15) and (2.16), the output Stokes power, the reflected pump power, and the transmitted pump power are found to be

$$P_{\text{out}} = \frac{\lambda_p}{\lambda_s} T_{s,\,\text{tot}} \left[\left(\frac{4\,T_{p,0}\,P_1 P_{\text{inc}}}{1 - R_{s,\,\text{rt}}}\right)^{1/2} - P_1(1 - R_{p,\,\text{rt}})\right], \tag{2.22}$$

$$P_{\text{refl}} = \left\{[P_1(1 - R_{s,\,\text{rt}})T_{p,0}]^{1/2} - \sqrt{P_{\text{inc}}}\right\}^2, \tag{2.23}$$

$$P_{\text{trans}} = P_1(1 - R_{s,\,\text{rt}})T_{p,1}, \tag{2.24}$$

where $T_{s,\,\text{tot}} = T_{s,0} + 3T_{s,1}$ for the ring cavity. The overwhelming similarities between these equations and those of the non-degenerate parametric oscillator are discussed in Chapter 3. One can also derive the previous three expressions for the emitted powers from the work of Repasky (aside from a factor of 2 error) [41], Peterson [43], and Brasseur [27] when modified for the ring cavity and in the appropriate limits. Interestingly, it is shown at the end of Appendix B that Eqs. (2.22) - (2.24) can also be directly applied to the two-mirror linear cavity with $T_{s,\,\text{tot}} = T_{s,0} + T_{s,1}$ and $R_{\text{rt}} = R_0 R_1$.

Using Eq. (2.17) for the threshold pump power, a handy dimensionless pumping ratio can be defined as

$$r_p \equiv \frac{P_{\text{inc}}}{P_{\text{th}}}. \tag{2.25}$$

So r_p, called the pump rate, represents the incident pump power normalized to the

threshold power. In terms of pump rate, Eqs. (2.22) and (2.23) can be recast as

$$P_{\text{out}} = \frac{\lambda_p}{\lambda_s} P_1 T_{s,\,\text{tot}} (1 - R_{p,\,\text{rt}}) \left(\sqrt{r_p} - 1\right) \tag{2.26}$$

$$P_{\text{refl}} = P_{\text{th}} \left(\frac{2T_{p,0}}{1 - R_{p,\,\text{rt}}} - \sqrt{r_p} \right)^2 . \tag{2.27}$$

The transmitted pump and output Stokes power from Eqs. (2.24) and (2.26) are plotted in Fig. 9(a) as functions of pump rate. Note the clamping of the transmitted pump power and the square-root dependence of the Stokes power on pump rate above threshold. This dependence is strictly a result of the cavity. The emitted Stokes power is linear when plotted versus the pump power that actually enters the cavity (i.e. that which is not reflected off the input coupler).

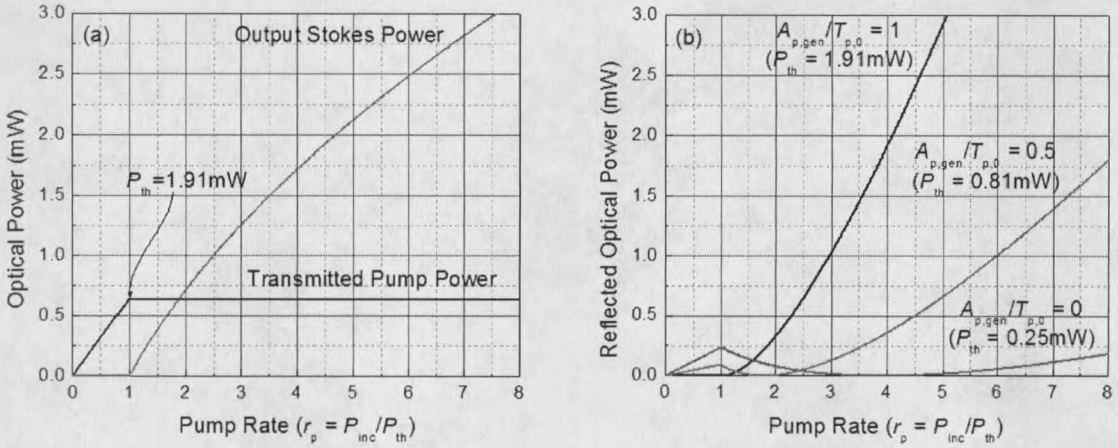

Figure 9. (a) Emitted and (b) reflected powers from the cw Raman laser cavity versus pump rate. The transmitted pump power is clamped above threshold ($r_p = 1$), while the emitted Stokes power exhibits a square-root dependence on the pump rate. By increasing the input coupler transmissivity ($T_{p,0}$) relative to the other intracavity losses at the pump wavelength ($A_{p,\,\text{gen}}$) impedance matching can occur above threshold, but not greater than four times threshold. The parameters used to generate these curves are: $P_1 = 24\text{kW}$, $R_{p,0} = R_{s,0}^3 = 0.9998$, $T_{p,0} = 200\text{ppm}$, and $R_{p,1} = R_{s,1}^3 = 0.9998$.

The first curve in Fig. 9(b) shows the reflected pump power from Eq. (2.27) for the same parameters. The other two curves in Fig. 9(b) will be discussed in the next subsection.

Impedance-Matching Power

Eq. (2.23) can be used to determine the pump power for which the active cavity is impedance matched; that is, the input pump power for which the reflected pump power vanishes [17, page 423]. Setting Eq. (2.23) to zero gives

$$\begin{aligned} P_{\text{match}} &= P_1(1 - R_{s,\,\text{rt}})T_{p,0} \\ &= 4P_{\text{th}}\left(\frac{T_{p,0}}{1 - R_{p,\,\text{rt}}}\right)^2 \qquad (2.28) \\ &\approx \frac{4P_{\text{th}}}{(1 + A_{p,\,\text{gen}}/T_{p,0})^2}, \qquad (2.29) \end{aligned}$$

where

$$\begin{aligned} R_{p,\,\text{rt}} &= R_{p,0}R_{p,1}^3 \\ &= (1 - T_{p,0} - A_{p,0})(1 - T_{p,1} - A_{p,1})^3 \\ &\approx 1 - T_{p,0} - A_{p,0} - 3T_{p,1} - 3A_{p,1} \\ &= 1 - T_{p,0} - A_{p,\,\text{gen}}. \qquad (2.30) \end{aligned}$$

Here, the A's are mirror power absorption coefficients and the generalized absorption is defined as

$$A_{p,\,\text{gen}} \equiv A_{p,0} + 3T_{p,1} + 3A_{p,1}. \qquad (2.31)$$

Approximation (2.29) shows that the pump power required to reach the impedance-matching condition approaches $4 \times P_{\text{th}}$ ($r_p = 4$) in the limit of small generalized absorptions. Fig. 9(b) shows the reflected power for three different choices of the ratio $A_{p,\,\text{gen}}/T_{p,0}$. As the ratio decreases, impedance matching occurs for higher input pump rates, meaning more and more pump light can enter the cavity for Raman conversion. However, the impedance-matching pump rate can never exceed $r_p = 4$. As will soon be shown, this particular pump rate is also (not coincidentally) significant for the system's conversion efficiency.

The impedance-matching phenomenon can be explained from a physical standpoint. For an *empty* cavity, no optical power is reflected when the input coupler losses exactly equal the other mirror losses [17, page 423]. This is because the portion of the circulating intracavity field that is transmitted back through the input coupler exactly cancels the portion of the incident field that is reflected from this mirror (they are out of phase). All the light is transmitted through an impedance-matched empty cavity with no absorptions.

However, for the *active* laser cavity currently under investigation, the circulating pump power is clamped by the Raman process above threshold. This means that the transmitted portion of the circulating field no longer perfectly cancels the reflected portion of the incident field. As a result, some optical power is reflected off the input coupler above threshold and is therefore not available for Raman conversion.

This problem is not unique to the cw Raman laser and is faced in every cavity-enhanced nonlinear process. The solution is to increase the transmissivity of the input coupler relative to the other intracavity losses at the pump wavelength. This means that incomplete cancellation of the two fields occurs *below* threshold (the transmitted intracavity portion is initially larger than the reflected incident portion), but that perfect cancellation will occur for one specific incident pump power value *above* threshold, as shown in the lower two curves of Fig. 9(b).

Raman Laser Optimization

This section is devoted to finding the optimal operation and construction parameters for the cw Raman laser. Note that the results of this section will not hold when thermo-optic effects are significant. The derivation process simply consists of taking derivatives with respect to the parameter of interest, setting to zero, and solving for the parameter. A useful equation for this purpose will be that of the photon conversion, or extraction efficiency, which is related to the ratio of the output to input powers through

$$\begin{aligned}\eta_{\mathrm{ph}} &\equiv \frac{\lambda_s}{\lambda_p}\frac{P_{\mathrm{out}}}{P_{\mathrm{inc}}} \\ &= \frac{T_{s,\mathrm{tot}}}{P_{\mathrm{inc}}}\left[\left(\frac{4\,T_{p,0}P_1P_{\mathrm{inc}}}{1-R_{s,\mathrm{rt}}}\right)^{1/2} - P_1(1-R_{p,\mathrm{rt}})\right]\end{aligned} \tag{2.32}$$

As a function of pump rate, this equation can be written

$$\eta_{\mathrm{ph}} = \left(\frac{T_{p,0}}{1-R_{p,\mathrm{rt}}}\right)\left(\frac{T_{s,\mathrm{tot}}}{1-R_{s,\mathrm{rt}}}\right)\left(\frac{1}{\sqrt{r_p}} - \frac{1}{r_p}\right). \tag{2.33}$$

With these equations, the photon extraction efficiency can now be optimized with respect to the pump rate.

Optimum Pump Rate

Differentiating Eq. (2.33) with respect to the pump rate, setting to zero, and solving for the optimum pump rate quickly yields

$$r_{p,\,\mathrm{opt}} = 4, \qquad \text{or equivalently} \qquad P_{\mathrm{opt}} = 4 \times P_{\mathrm{th}}. \tag{2.34}$$

This indicates that, regardless of mirror absorptions, transmissions, Raman gain, or cavity geometry, the optimal pump rate is always $r_{p,\,\mathrm{opt}} = 4$. It is interesting that the impedance-matched condition approaches this optimal pump rate for high $T_{p,0}$. Inserting $r_{p,\,\mathrm{opt}} = 4$ into Eq. (2.33) and only considering Stokes power emitted from the output coupler gives the optimum usable photon conversion efficiency

$$\eta_{\mathrm{ph,\,opt}} \equiv \frac{\lambda_s}{\lambda_p}\frac{P_{\mathrm{out}}}{4P_{\mathrm{th}}} \approx \left(1 + \frac{A_{p,\,\mathrm{gen}}}{T_{p,0}}\right)^{-1}\left(1 + \frac{A_{s,\,\mathrm{gen}}}{T_{s,0}}\right)^{-1}, \tag{2.35}$$

which approaches unity in the limit of small generalized absorptions, where the generalized absorption terms $A_{p,\mathrm{gen}}$ and $A_{s,\,\mathrm{gen}}$ are of the form given in Eq. (2.31). This is an important result because it states that the only parameters that limit the conversion efficiency for cw Raman lasers are the ratios of the generalized absorptions to the input/output coupler transmissions at the two wavelengths. Eq. (2.35) as well as the results to follow can be modified to include all the output Stokes power (not just that emitted out the input coupler) by setting $A_{s,\,\mathrm{gen}} \rightarrow A_{s,\,\mathrm{tot}}$ and $T_{s,0} \rightarrow T_{s,\,\mathrm{tot}}$.

Optimum Input and Output Coupling

The choice of mirror transmissions for optimum power extraction is now discussed. In this case, it is assumed that the maximum amount of incident pump power available is a fixed quantity ($P_{\max}$) and the input and output coupling coefficients are determined in order to optimize the Stokes power extraction. Because $T_{p,1}$ and $T_{s,1}$ enter equivalent to absorptions in Eq. (2.35), these transmissivities should clearly be chosen as low as possible (this can be proven more rigorously). This allows $T_{p,0}$ and $T_{s,0}$ to be considered as the only optimization parameters. It is now possible to determine whether there is any advantage to be gained by choosing the the mirror transmissivities higher for one wavelength than the other and what the values must be to optimize the Stokes power extraction. Specifically, by differentiating Eq. (2.32) once with respect to $T_{p,0}$ and again with respect to $T_{s,0}$, the resulting two equations can be set to zero and solved simultaneously for the transmissions to yield

$$T_{p,0,\,\mathrm{opt}} = \sqrt{\frac{A_{p,\,\mathrm{gen}}}{A_{s,\,\mathrm{gen}}}\frac{P_{\max}}{P_1}} \tag{2.36}$$

$$T_{s,0,\,\mathrm{opt}} = \sqrt{\frac{A_{s,\,\mathrm{gen}}}{A_{p,\,\mathrm{gen}}}\frac{P_{\max}}{P_1}} - A_{s,\,\mathrm{gen}}. \tag{2.37}$$

Interestingly, these equations indicate that, to extract the most power from the system, the transmission coefficients for the input/output coupler will in general be different for the two wavelengths. One might be tempted to assume that these transmission coefficients should reproduce the condition $P_{\max} = 4 \times P_{\mathrm{th}}$ (i.e. satisfy the four-times-threshold condition). However, when Eqs. (2.36) and (2.37) are inserted

into Eq. (2.17) the result is

$$P_{\text{th, opt}} = \frac{P_{\max}}{4}\left[1 + \left(\frac{4\,P_1}{P_{\max}} A_{p,\,\text{gen}} A_{s,\,\text{gen}}\right)^{1/2}\right], \tag{2.38}$$

which indicates that the optimum threshold is slightly larger than $P_{\max}/4$. In other words, the optimum input/output coupling is such that the system will run slightly *under* the four-times-threshold condition when the maximum incident pump power is used. This seems to contradict the findings of the previous subsection. However, one must remember that the four-times-threshold condition optimizes the power extraction efficiency with respect to pump rate rather than mirror transmissions.

Figure 10 helps to further clarify this issue. The figure shows the photon conversion efficiencies for three different choices of transmission coefficients, as functions of the pump rate for the curve labeled A. In other words, the incident pump powers for all the curves are normalized to the threshold of curve A. The vertical dashed line represents the maximum available pump power. Pump powers greater than this ($r_p^{(A)} > 4$) are therefore inaccessible to the system. Curve A represents a choice for mirror transmissions such that $P_{\max} = 4 \times P_{\text{th}}$. Note that the conversion efficiency peaks at $P_{\max}$ as predicted by Eq. (2.34). However, by increasing the output coupling coefficient (and thereby raising the threshold) while holding all other parameters constant, one can increase the conversion efficiency from the previous situation even though this means that the conversion efficiency does not peak with respect to incident pump power. Curve B represents the optimal mirror transmissions calculated

using Eqs. (2.36) and (2.37). Curve C shows that any further increase in the output transmission beyond the optimal values again results in a reduced conversion efficiency.

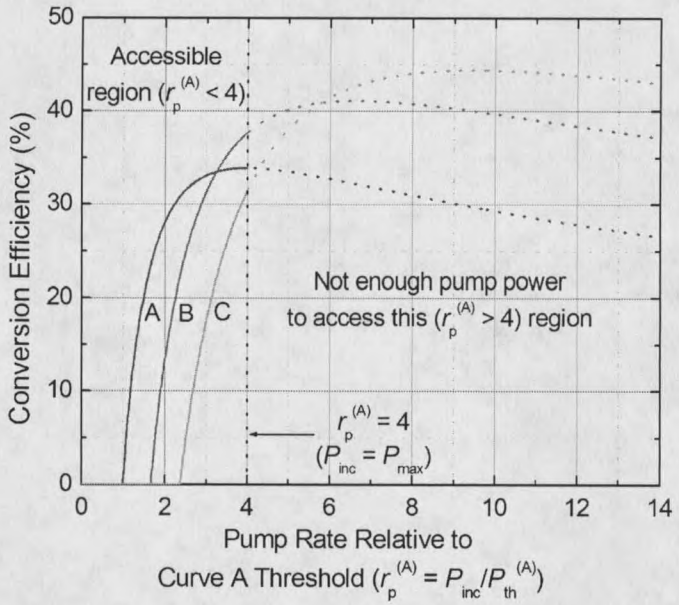

Figure 10. Photon conversion efficiency versus the pump rate relative to the curve A threshold. The mirror transmissivities for curve A are chosen such that the threshold occurs at 1/4 of the maximum available pump power. The transmissivities for curve B are chosen according to Eqs. (2.36) and (2.37) and maximize the conversion efficiency for the available pump power.

In practice, more pressing concerns usually dominate the choice of mirror reflectivities. First off, it must be emphasized that the effect just described is only significant when the mirror absorptions are comparable or larger than the input/output transmission coefficient. Also, obtaining mirrors that are coated with the required accuracy for two wavelengths can be difficult and expensive. Nevertheless, Research

Electro-Optics (REO) in Boulder, Colorado can coat mirrors with transmission accuracy better than 95%. But perhaps more importantly, as discussed in the next two chapters, the input/output transmission coefficients should be chosen larger for the pump than for the Stokes for the purposes of stability, regardless of power extraction efficiency.

Optimum Detuning

A very useful physical picture of cw Raman laser frequency tuning is given in Appendix D. To this point in the chapter, it has been assumed that the pump and Stokes cavity modes differ in frequency by precisely the Raman shift. In other words, the HFC length is adjusted such that the Stokes cavity mode falls directly on the line center of the Raman transition (see Fig. 63 in Appendix D). Frequency tuning of the Raman laser away from this situation can yield some interesting behavior and was first addressed in Ref. [28]. For optimization purposes, detuning of the Stokes cavity mode from the Raman gain line center can be incorporated into all of the previous equations using the following simple transformation:

$$P_1 \rightarrow \frac{P_1}{\mathcal{L}(\Delta_{12})}, \tag{2.39}$$

where

$$\mathcal{L}(\Delta_{12}) = \frac{\gamma_{21}^2}{(2\Delta_{12})^2 + \gamma_{21}^2} \tag{2.40}$$

is the Lorentzian lineshape of the Raman transition in the high-pressure limit [48]. Here, $\Delta_{12} \equiv \omega_p - \omega_s - \omega_{21}$ is the detuning from the transition line center, where

ω_p, ω_s, and ω_{21} are the pump, Stokes, and vibrational frequencies, respectively. The constant γ_{21} represents the full width at the half maximum of the Raman gain. This treatment assumes that no mode hops (spatial, longitudinal or directional) occur during the tuning.

With Eq. (2.39) included, Eq. (2.32) can be differentiated with respect to the detuning Δ_{12}. The result can be set to zero and solved for the optimal detuning to yield

$$\Delta_{12,\,\mathrm{opt}} = 0 \qquad (\, r_p \leq 4) \tag{2.41}$$

$$= \pm\frac{\gamma_{21}}{2}\sqrt{\frac{P_{\mathrm{inc}}}{4P_{\mathrm{th}}} - 1}. \qquad (\, r_p > 4) \tag{2.42}$$

Figure 11(a) shows the output powers versus detuning for four different choices of pump rate (2, 4, 6, and 8). For a pump rate of $r_p = 8$, the Stokes power peaks at $\pm\gamma_{21}/2$ as predicted by Eq. (2.42). Figure 11(b) illustrates the bifurcation predicted by Eqs. (2.41) and (2.42) with increasing pump rate. Note also that for pump rates between $r_p \approx 4$ and $r_p \approx 6$, the Stokes power output is nearly constant with detuning out to about $\pm\gamma_{21}/2$. This feature can be used to determine the maximum constant power detuning as discussed in Appendix D.

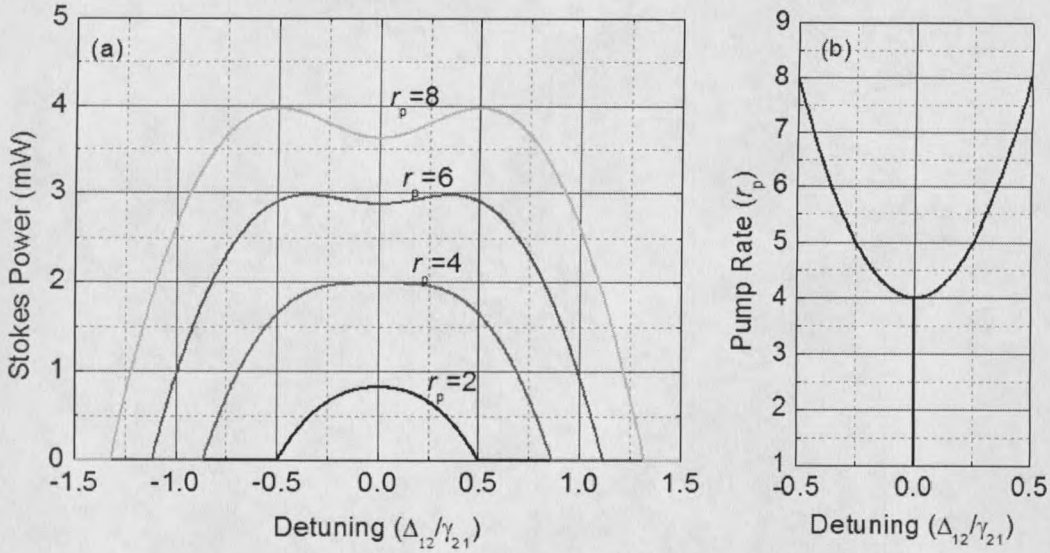

Figure 11. (a) Stokes output power versus detuning from the two-photon Raman transition line center (Δ_{12}) for several different pump rates. (b) Optimum detuning (horizontal axis) versus pump rate (vertical axis).

Although the tuning behavior for $r_p > 4$ resembles a Lamb dip, the cause is physically unrelated. The Lamb dip occurs due to Doppler broadened gain media in standing-wave laser cavities, as discussed in Ref. [17, pages 1199-1212]. The dip in the Raman output power is due to the fact that the peak in the conversion efficiency occurs at $r_p = 4$. By tuning away from the Raman line center, the Raman gain drops, thus raising the effective threshold. Therefore, when $r_p > 4$ on the line center, detuning takes the system *closer* to $r_p = 4$, thereby increasing the conversion efficiency.

Optimum Cavity Geometry

Because the optimum power extraction efficiency is independent of P_1, it is therefore independent of the cavity geometry. This ceases to be true when the medium is

depleted or nonlinear refractive index effects (such as heating) are significant. Regardless, P_1 does play a role in determining the laser threshold. Using the trigonometric relation [49, page 467]

$$\csc^{-1}(x) = \tan^{-1}\left(\frac{1}{\sqrt{x^2-1}}\right),$$

Eq. (2.10) can be recast as

$$P_1 \equiv \frac{\lambda_p + \lambda_s}{16\alpha \csc^{-1}\sqrt{2R/L}} \tag{2.43}$$

where R is the mirror radius of curvature and the following relation for the confocal parameter of a cavity has been used [50, page 140]

$$b = L\sqrt{\frac{2R}{L} - 1}. \tag{2.44}$$

To most effectively utilize the Raman gain, one can therefore maximize the inverse cosecant in Eq. (2.43). This function is plotted versus R/L in Fig. 12. Two well-known cavity geometries (the concentric and the confocal) are indicated on the plot by solid circles and the open squares indicate R/L ratios that have been used successfully.

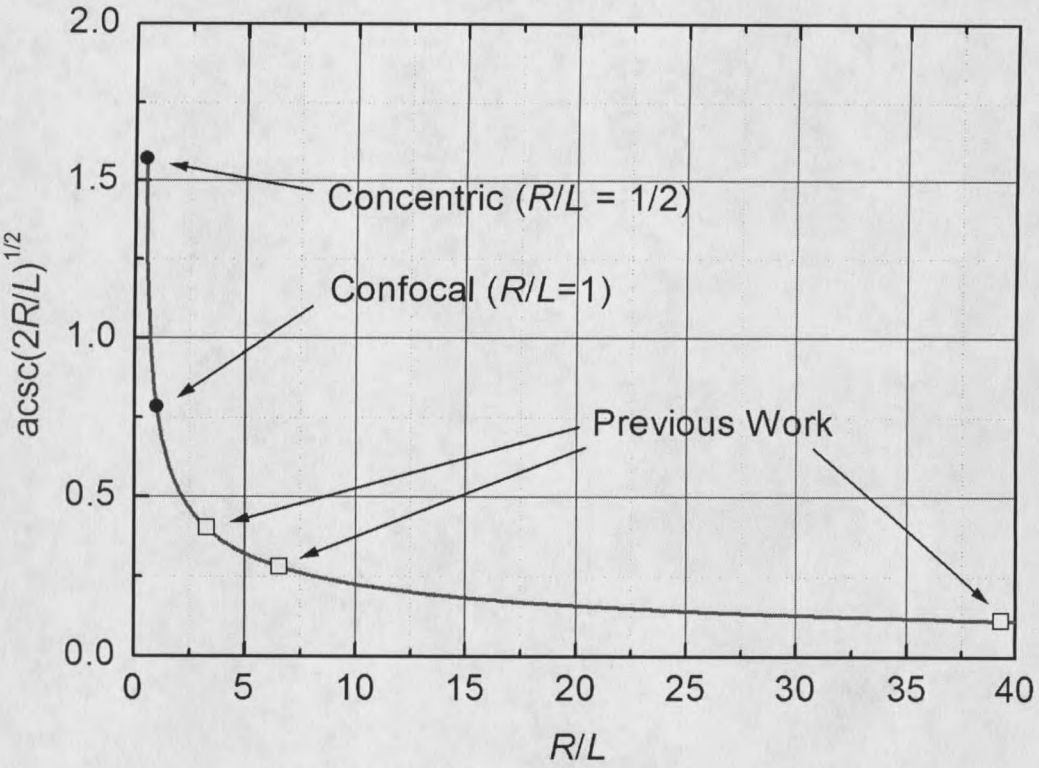

Figure 12. Inverse cosecant function (which is proportional to the focused gain) as a function of curvature-to-length ratio (R/L). The figure suggests that the concentric cavity geometry is optimal, but practical concerns favor other geometries.

The figure suggests that the concentric geometry should minimize the threshold, but practical concerns again dominate the choice of R/L. Specifically, as discussed by Boyd in Ref. [40], R/L values near unity "place a premium on the quality of the mirrors" because the beam spot size on the mirrors is so large. Nonuniformities in the mirror surfaces over large areas can degrade the cavity finesse. I have not investigated such deleterious effects, but other researchers have used a 1mm spot size and retained a cavity finesse of 150,000 using mirrors from REO [51]. Boyd also points out that "in the degenerate case the spatial nonuniformity of Stokes gain results in a parametric

coupling of the simultaneously resonant transverse modes." Thus one may want to avoid rational fractions for R/L such as 1 (confocal), 2/3, 3/2, etc.

Chapter Summary

This chapter has been devoted to developing the cw Raman laser theory in a manner that hopefully facilitates basic understanding of the system. Equations (2.13) and (2.14) gave the time dependent, coupled behavior of the circulating pump and Stokes powers. The conditions for the laser threshold and impedance matching were given in Eqs. (2.17) and (2.28). Perhaps most useful were Eqs. (2.22) - (2.24), which gave the steady-state output powers. It was also shown that the optimal pump rate is four times the threshold value and that the peak photon conversion efficiency can approach 100% in the limit of small generalized absorptions (which include all transmissions other than the input/output coupler). Optimization was also performed with respect to the input/output coupling, detuning from the Raman line-center, and cavity geometry. In the next chapter, the emphasis shifts from simplicity toward rigor as the quantum mechanical aspects of the cw Raman laser are addressed.

CHAPTER 3

QUANTUM THEORY

The primary goal of this chapter is to provide detailed insight into the quantum mechanical processes involved with cw Raman lasing. The work presented here is the result of the better part of a wonderful year spent in Australia interacting with Tim Ralph and Andrew White, both of whom were at the University of Queensland.

Rather than simplifying matters by assuming a real, non-transient, macroscopic polarization that only includes the Raman process as I did in Appendix B, I now start with a more fundamental microscopic picture of the underlying atomic structure and allow the physical system itself to determine any simplifications. And instead of treating the optical modes as fields that can assume any value of energy, I start with quantized cavity modes so that their energies are discretized and exchanges of energy must involve the creation or annihilation of a photon. By the end, this treatment allows for determination of all the populations, both the fields, and the intensity noise behavior of the emitted light with quantum noise included. The system is eventually shown to be capable of exhibiting intensity noise below the standard quantum limit (amplitude squeezing) for certain operating conditions. Along the way, an interesting and useful connection is uncovered between the far-off-resonance cw Raman laser and

the nondegenerate optical parametric oscillator (NDOPO). Additionally, the analysis given here lends itself naturally to investigation of parametric anti-Stokes and second-Stokes generation. A streamlined treatment of anti-Stokes generation in the semiclassical limit is provided in Appendix G.

This chapter begins with a review of past quantum mechanical treatments of related systems to provide context. The second section is used to assemble the appropriate components of the Hamiltonian for the far-off-resonance cw Raman laser system at hand. Due to the extraordinarily large detunings present in this system, the rotating wave approximation (RWA) is not valid, and is therefore not invoked. The quantum Langevin equations for the system operators are generated in the third section following the work of Gardiner and Collett [52]. In the fourth section, the large single-photon detuning is exploited to simplify the equations of motion significantly. In the fifth section, the semiclassical limit of the quantum Langevin equations is taken and the results are compared to the previous chapter. Returning to the quantum domain in the sixth section, direct connections are drawn between the cw Raman system and the NDOPO. In the seventh section, the simplified quantum Langevin equations for the two fields are linearized and the noise spectra of the emitted Stokes light is determined analytically. The eighth section is used to analyze and explore the parameter space of these equations. The final section consolidates the work of this chapter. Throughout this chapter, I attempt to follow the notation of Gardiner and Zoller [53].

The appendices associated with this chapter are provided primarily to supplement

large mathematical gaps in the main chapter. However, Appendix G documents the development of the semiclassical anti-Stokes theory when cavity enhancement of the anti-Stokes field is included. It is shown that the photon conversion efficiency can approach the quantum limit of 50% under ideal experimental conditions.

Previous Work

The literature addressing the quantum mechanical nature of pulsed Raman systems is prodigious, [54, and references therein] but little attention was devoted to the cw regime until the late 1980's and the 1990's, when three-level atoms interacting with quantized field modes were analyzed in the process of identifying and characterizing nonclassical sources of light. For such atoms in the Λ-configuration, many competing processes (including Raman) often contribute to the overall dynamics of the system. The dominance of certain processes over others is determined by the relative strengths of the rates involved (decay rates, detunings, Rabi frequencies, etc.) and the pumping scheme (coherent versus incoherent).

In particular, three level Λ-systems can exhibit optical bistability [55, and references therein] traditional population-based lasing (see, for example, Ref. [56], lasing without inversion [57, 58, 59], electromagnetically induced transparency [60, and references therein] in addition to Raman lasing [61, 62, 63, 64]. General treatments of three level systems have also been performed, which can accommodate many of these processes [65, 66, 67, 68]. All of the specifically Raman laser studies mentioned

above address the case where no decay path to the ground state is included to close the pump cycle. In these systems, the middle level population returns to the ground state via coherent interactions with the cavity fields (anti-Stokes process). On the other hand, Ritsch, *et al.* [65, 66] as well as others [67, 68] accommodate decay to the ground state as part of the pump cycle. These works provide useful general treatments of three level systems interacting with two cavity modes in the Schrödinger picture. Presumably none of them dealt with detunings large enough to become incompatible with the rotating wave approximation (RWA) since it was invoked in all.

The present treatment is directly based on the far-off-resonance cw Raman laser systems that have been experimentally realized [69, and references therein]. Specifically, this treatment assumes a collection of diatomic hydrogen molecules (approximated by three-level systems in the Λ-configuration) interacting with two strongly cavity-enhanced field operators. The field operators are very far detuned in frequency from the single-photon transitions, so the RWA is not invoked. Decay of all the level populations and coherences is allowed. In this treatment, the single-photon detunings are by far the largest rates in the system. The energy level diagram and specific descriptions of the interactions are included in the next section.

Another closely related work is that of Poizat, *et al.* [70] who examine two field modes interacting with a system of three-level atoms in a ladder or cascade configuration. It is pointed out by Olsen *et al.* [71] that this system can behave very similar to the corresponding Λ-configuration under similar conditions.

Hamiltonian

In the interest of retaining as much clarity as possible, attention will be focused on the temporal aspects of the system in this work and only a nonrigorous treatment of the spatial dependence will be provided. Also for simplicity, the cavity is assumed to be lossless and single-ended (i.e. only the input/output coupler has a reflectivity less than unity), but other mirror transmissions and losses can easily be included using the same formalism [72, and references therein]. It should be noted that thermal population of the pertinent excited states is negligible for the system at hand because they differ in energy from the ground state by more than $20 \times k_B T$. The generation of anti-Stokes radiation is neglected in the main text because it is very small in practice [30] and does not appreciably affect the dynamics of the other fields when it is not cavity enhanced. The effect of cavity enhancing the anti-Stokes field is treated in Appendix G. The complicating effects of heat generation are diverted until the next chapter [29, 36].

The atom-photon interactions that are included in this treatment, and the corresponding energy level diagram, are somewhat unconventional due to the extreme single-photon detuning that exists. As shown in Fig. 13, the hydrogen molecule is approximated by a three-level system in the Λ-configuration where level 1 is the ground state, level 2 is the first excited vibrational state, and level 3 is the first excited electronic state. The figure shows these three levels and all the pertinent fields to-scale

in order to emphasize the large single-photon detunings. As a result of the large detunings, note that *both* the pump and Stokes fields are permitted to drive each of the two allowed single-photon transitions (1–3 and 2–3). Single-photon 1–2 transitions are forbidden by selection rules. Also note that the counter-rotating portions of each field are explicitly included and are represented by arrows below the energy levels. Detunings are represented by Δ's, the population decay rates by $\bar{\gamma}$'s and the collisional dephasing rates by $\tilde{\gamma}$'s (not shown in the figure). Due to the large single-photon detunings, the fields will interact with more upper levels than just the one shown, but it is assumed that these will all contribute in a similar manner.

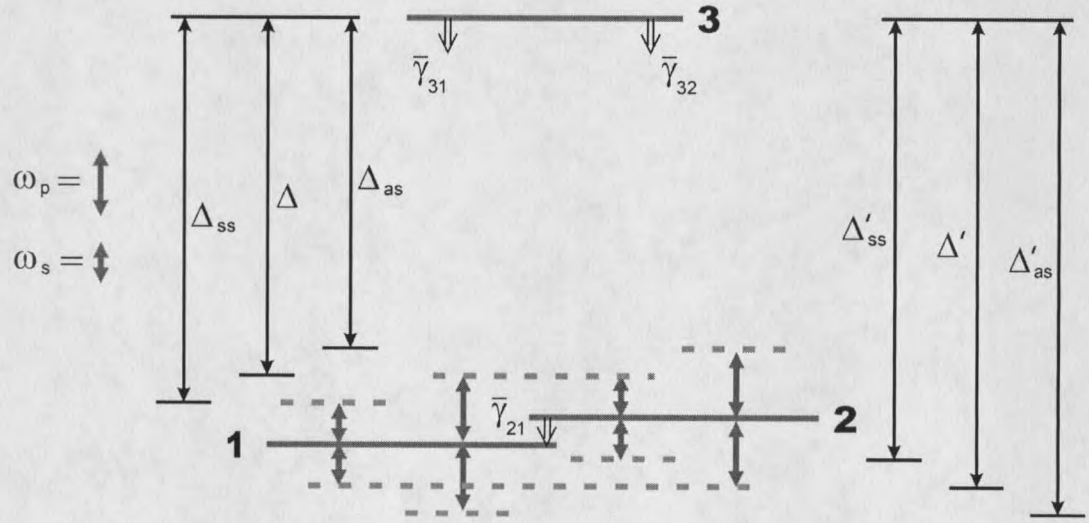

Figure 13. To-scale energy level diagram for the diatomic hydrogen molecule showing the pertinent levels and the far-off-resonance fields. The arrows below the energy levels represent counter-rotating terms that must be included due to the large single-photon detunings (Δ's).

The total Hamiltonian describing the atoms, the fields, the baths (to incorporate decay and noise), and their mutual interactions is

$$H = H_1 + H_2 + H_3 + H_4 + H_5 + H_{\text{baths}}, \tag{3.1}$$

where the components of H are given as follows.

Free Energy

H_1 represents the free energy of the atoms and fields in the absence of any interactions and is given by

$$H_1 = \sum_{i=1}^{3} \hbar\omega_i S_{ii} + \sum_{q=p,s} \hbar\omega_q^c a_q^\dagger a_q, \tag{3.2}$$

where $\hbar\omega_i$ and S_{ii} are the energy and collective population operator for the i-th atomic level, respectively. Throughout this work, the subscript p refers to the pump while s refers to the Stokes. In this way, the operators a_q and $a_q^\dagger$ refer to the annihilation and creation of pump $(q = p)$ and Stokes $(q = s)$ photons, respectively, while ω_p^c and ω_s^c are the frequencies of the cold cavity modes nearest to the pump and Stokes laser frequencies, respectively.

Reversible Interaction Energy

H_2 represents the reversible interaction energy associated with the atom-field couplings in the electric dipole approximation and is given by

$$H_2 = i\hbar \sum_{q=p,s} (a_q^\dagger - a_q)\Big(g_{q,13}\, S_{13} + g_{q,23}\, S_{23} + \text{H.c.}\Big), \tag{3.3}$$

where H.c. denotes the Hermitian conjugate, the collective coherence operator between levels i and j is given by S_{ij}, and $g_{q,ij}$ represents atom-field coupling constant for the traveling wave field mode q driving the i–j atomic transition. This coupling constant is given by

$$g_{q,ij} = \frac{\mu_{ij}}{\hbar}\sqrt{\frac{\hbar\omega_q}{2\epsilon_0 V_q}}, \tag{3.4}$$

where μ_{ij} is the dipole matrix element between levels i and j, and V_q is the effective volume of the q-th fundamental cavity mode. Note that Eq. (3.3) includes the interaction energy associated with *both* fields driving each of the two allowed transitions. Moreover, it includes the counter-rotating terms associated with each field. This is in contrast to the case of near-resonance interactions where the counter-rotating terms, which do not "conserve energy" (so to speak), are neglected in the RWA as discussed by Scully and Zubairy [73, page 196] as well as Orszag [74, page 84]. In the present case, all of the terms are horrendously detuned and are therefore similarly abysmal in their (lack of) energy conservation. This severely decreases the probability for the transitions involved and also dictates that no single field component will dominate the interaction. They shall all, therefore, be retained.

Irreversible Interaction Energy

H_3 represents the coupling between the two active cavity modes and the external

field baths for decay and noise purposes and is given by

$$H_3 = i\hbar \sum_{q=p,s} \int_{-\infty}^{\infty} d\omega \sqrt{\frac{\kappa_q}{\pi}} \left[b_q^\dagger(\omega) a_q - a_q^\dagger b_q(\omega) \right], \tag{3.5}$$

where the external field bath operators, b_q and $b_q^\dagger$, are coupled to the q-th internal mode of the cavity through the (amplitude) cavity decay rate κ_q. The decay rate, and therefore the mirror reflectivity for each mode is assumed to be constant over a large frequency bandwidth compared to the cavity resonance (the first Markoff approximation), which is easily achieved in practice. Mirror absorptions can be included in direct analogy with Eq. (3.5) [72].

H_4 represents the coupling between atomic coherences and atomic bath operators to generate damping and noise in the atoms and is given by

$$\begin{aligned} H_4 = i\hbar \int_{-\infty}^{\infty} d\omega \Bigg\{ & \sqrt{\frac{\bar{\gamma}_{21}}{2\pi}} \left[B_{12}^\dagger(\omega) S_{12} - S_{12}^\dagger B_{12}(\omega) \right] \\ & + \sqrt{\frac{\bar{\gamma}_{31}}{2\pi}} \left[B_{13}^\dagger(\omega) S_{13} - S_{13}^\dagger B_{13}(\omega) \right] \\ & + \sqrt{\frac{\bar{\gamma}_{32}}{2\pi}} \left[B_{23}^\dagger(\omega) S_{23} - S_{23}^\dagger B_{23}(\omega) \right] \Bigg\}, \end{aligned} \tag{3.6}$$

where the the decay rates of the level populations, given by the $\bar{\gamma}_{ji}$'s, can be interpreted as coupling constants between the system operators and the atomic bath operators, which are given by B_{ij} and $B_{ij}^\dagger$. It has again been assumed that the decay rates are constant over a large frequency bandwidth compared to the atomic resonances (the first Markoff approximation). Population decay downward from levels 2 and 3 is assumed to be due to inelastic molecular collisions and spontaneous emission, respectively.

Similarly, H_5 represents the coupling between atomic populations and atomic bath operators to generate decay and noise of the atomic coherences through dephasing and is given by

$$H_5 = i\hbar \sum_{i=1}^{3} \int_{-\infty}^{\infty} d\omega \sqrt{\frac{\tilde{\gamma}_{ii}}{2\pi}} \Big[B_{ii}^{\dagger}(\omega) S_{ii} - S_{ii} B_{ii}(\omega) \Big], \tag{3.7}$$

where the $\tilde{\gamma}_{ii}$'s are the dephasing rates associated with each level due to elastic collisions, while $B_{ii}^{\dagger}$ and B_{ii} are the corresponding atomic bath operators. This interaction is modeled after Gardiner and Zoller [53] and Eschmann *et al.* [68].

Bath Energy

Finally, H_{baths} represents the free energy of the external bath or reservoir modes (one operator for each decay path available to the system) and is given by

$$\begin{aligned} H_{\text{baths}} = & \sum_{q=p,s} \int_{-\infty}^{\infty} dw\, \hbar\omega\, b_q^{\dagger}(\omega) b_q(\omega) \\ & + \int_{-\infty}^{\infty} dw\, \hbar\omega \Big[B_{12}^{\dagger}(\omega) B_{12}(\omega) + B_{13}^{\dagger}(\omega) B_{13}(\omega) + B_{23}^{\dagger}(\omega) B_{23}(\omega) \Big] \\ & + \sum_{i=1}^{3} \int_{-\infty}^{\infty} dw\, \hbar\omega\, B_{ii}^{\dagger}(\omega) B_{ii}(\omega). \end{aligned} \tag{3.8}$$

The above components of H do not deviate drastically from previous treatments aside from the reversible interaction energy H_2, which includes several additional terms due to the large single-photon detunings.

Multiplications and Commutations

The following sum will be referred to as the "system" Hamiltonian

$$H_{\text{sys}} = H_1 + H_2. \tag{3.9}$$

This is the portion of the total Hamiltonian that does not include the reservoirs or their interactions with the atoms and fields inside the cavity. The system operators are therefore the cavity field operators as well as the population and coherence operators. They obey the following standard equal-time commutation relations and multiplication rules

$$[a_q, a_{q'}^\dagger] = \delta_{qq'}, \qquad S_{ij}S_{kl} = S_{il}\,\delta_{jk}, \qquad [S_{ij}, S_{kl}] = S_{il}\,\delta_{jk} - S_{jk}^\dagger\,\delta_{il}, \tag{3.10}$$

where it should be noted that $S_{jk}^\dagger = S_{kj}$. The reservoir operators obey standard boson commutation relations.

In the Heisenberg picture, one can now use the above Hamiltonian and commutation relations to generate the quantum Langevin equations for the system operators. An alternative approach is to proceed in the Schrödinger picture and generate a master equation for the time dependence of the density matrix. The benefits and drawbacks of these two approaches are discussed in Ref. [75].

Quantum Langevin Equations

In this section, the Heisenberg equation of motion is used to generate Langevin equations for the system operators. Unfortunately, as will become evident, the choice not to use the RWA complicates matters when converting to rotating coordinate frames. The crux of the problem lies in the fact that the (non-RWA) coherences are composed of multiple Fourier frequencies rather than just one. This means that there is no single coordinate frame to which one can transform in order to produce the

desired slowly varying coherence coefficients (one Fourier component will be slowly varying but the others will not). Fortunately, the Fourier components are spectrally separated by optical frequencies so that one can assume there is no mutual interaction. This allows a Langevin equation to be generated for each independent Fourier component of the S_{13} and S_{23} coherence operators. For reasons discussed below, this is not an issue for the two-photon coherence (S_{12}), the populations, or the fields, and they are readily converted to rotating frames. It must also be stated here that the equations generated in this section are undeniably nasty, but they can be interpreted from physical standpoints and are greatly simplified in the following section.

Heisenberg Equation of Motion

Using the Hamiltonian and commutation relations from the previous section, one can now calculate the quantum Langevin equations using the Heisenberg equation of motion. This procedure is greatly facilitated by the work of Gardiner and Collett [52] who showed that the Heisenberg equation of motion can take the form

$$\dot{a}_p = -\frac{i}{\hbar}[a_p, H_{\text{sys}}] - \sum_{j=1}^{8}[a_p, c_j^\dagger]\left\{\frac{\gamma_j}{2}c_j - \sqrt{\gamma_j}\, b_j^{\text{in}}(t)\right\} + \sum_{j=1}^{8}\left\{\frac{\gamma_j}{2}c_j^\dagger - \sqrt{\gamma_j}\, b_j^{\text{in}\dagger}(t)\right\}[a_p, c_j] \tag{3.11}$$

for the pump field operator, for instance. The equations for the other system operators are obtained by simply replacing a_p with the desired system operator. The first term on the right side accounts for the free evolution and reversible interactions of the system operators, whereas the last two terms generate decay and noise of the system

operators through irreversible interactions with the reservoirs from H_4 and H_5 of the previous section.

The elements of the array $\mathbf{c}$, which are indexed with the subscript j, include the system operators that are coupled to external reservoir operators, with the array given by

$$\mathbf{c} = (a_p, a_s, S_{12}, S_{13}, S_{23}, S_{11}, S_{22}, S_{33}). \tag{3.12}$$

This array includes all of the system operators for the system considered here because each of the eight system operators is coupled to one reservoir as described in the previous section. The γ_j's in Eq. (3.11) are the constants with which the system operators of $\mathbf{c}$ are coupled to the reservoir operators from Eqs. (3.5) - (3.7). The γ_j's also compose an array, which is given by

$$\gamma = (2\kappa_p, 2\kappa_s, \bar{\gamma}_{21}, \bar{\gamma}_{31}, \bar{\gamma}_{32}, \tilde{\gamma}_{11}, \tilde{\gamma}_{22}, \tilde{\gamma}_{33}). \tag{3.13}$$

As described in Ref. [52], the b_j^{in} 's are reservoir *input* operators that result from the system-reservoir coupling. The array of input operators is given by

$$\mathbf{b^{in}} = (a_p^{\text{in}}, a_s^{\text{in}}, B_{12}^{\text{in}}, B_{13}^{\text{in}}, B_{23}^{\text{in}}, B_{11}^{\text{in}}, B_{22}^{\text{in}}, B_{33}^{\text{in}}), \tag{3.14}$$

each component of which is defined in the following manner [76]

$$b_j^{\text{in}}(t) \equiv -\frac{1}{\sqrt{2\pi}} \int_{-\infty}^{\infty} dw\, e^{-i\omega(t-t_0)} b_j^0(\omega) \qquad (t > t_0), \tag{3.15}$$

where $b_j^0(\omega)$ is the value of $b_j(\omega)$ at $t = t_0$ with the corresponding reservoir operators

$b_j(\omega)$ given by the array

$$\mathbf{b} = (b_p, b_s, B_{12}, B_{13}, B_{23}, B_{11}, B_{22}, B_{33}). \tag{3.16}$$

Note that the input operators given in Eqs. (3.14) and (3.15) have units of $\sqrt{Hz}$ as opposed to the system operators, which are unitless. This is so the square of an input operator gives a photon flux (s^{-1}). It should also be pointed out that all of the input operators except for that of the pump represent stochastic noise inputs with zero expectation values (for instance, $\langle a_s^{\text{in}} \rangle = 0$). The pump field input operator is a bit different because it is assumed that there exists an input pump beam into the cavity. For this case, $\langle a_p^{\text{in}} \rangle = \alpha_p^{\text{in}} \sqrt{\tau_{\text{rt}}}$, where τ_{rt} is the round-trip time in the cavity and α_p^{in} is the unitless classical input pump field (a complex, or c-number; not an operator). The input operators obey the same mutual commutation relations as their reservoir counterparts, given by

$$[b_j^{\text{in}}(t)\,, b_{j'}^{\text{in}\,\dagger}(t')] = \delta_{jj'}\,\delta(t-t'). \tag{3.17}$$

However, it should be noted that although the reservoir operators (elements of $\mathbf{b}$) commute with the system operators at equal times, this is not necessarily true for the input operators (elements of $\mathbf{b^{in}}$), whose commutation relations are given in reference [52]. With the knowledge of the total Hamiltonian and all the pertinent commutation relations, Eq. (3.11) can be used to obtain a complete set of first order coupled differential equations for the system operators; the so-called quantum Langevin equations.

Rotating Coordinate Transformations

The standard next step is to use Eq. (3.11) to generate quantum Langevin equations of motion for the system operators. The operators are then transformed to rotating coordinate systems in order to extract the slowly varying behavior from the rapidly oscillating carrier frequencies.

In the present case, this procedure is straightforward for both of the field operators and for the 1–2 coherence operator. This is because the pump and Stokes field operators are very nearly resonant with the associated cavity modes ($\omega_p \approx \omega_p^c$ and $\omega_s \approx \omega_s^c$) and the two-photon Raman transition ($\omega_p - \omega_s \approx \omega_2 - \omega_1$). Therefore, each of the three operators will exhibit slowly varying behavior around a single carrier frequency that is close to the corresponding resonance. Fourier components that are detuned from the resonances by optical frequencies ($\sim$ 100THz) will be heavily attenuated because the cavity and Raman linewidths are $\sim$ 1MHz and $\sim$ 1GHz, respectively. These components can be ignored when compared to the resonant components. The validity of this assumption can be proven rigorously. One can therefore perform the simple transformations

$$a_p = a_p' e^{-i\omega_p t}, \qquad a_s = a_s' e^{-i\omega_s t}, \qquad \text{and} \qquad S_{12} = S_{12}' e^{-i(\omega_p - \omega_s)t} \tag{3.18}$$

to extract the slowly varying behavior (now contained in the primed operators) from the rapidly oscillating carrier frequencies. The associated noise operators are transformed similarly.

The situation is not so straightforward for the 1–3 and 2–3 coherence operators.

This is because the pump and Stokes field operators are not remotely resonant with the single-photon transitions ($\omega_p \neq \omega_3 - \omega_1$ and $\omega_s \neq \omega_3 - \omega_2$), as shown in Fig. 13. As a result, no carrier Fourier component dominates the interaction and all contribute significantly to the coherence. This means that there is no single rotating coordinate system to which one can transform S_{13} and S_{23} in order to extract the slowly varying behavior from the rapid carrier oscillations. A transformation directly following Eq. (3.18) will not produce a slowly varying coefficient because multiple carrier frequencies exist.

However, because the carrier frequencies differ from one another by optical frequencies, it is possible to treat the slowly varying behavior associated with each carrier frequency as a separate degree of freedom. As will become evident later in this section both S_{13} and S_{23} exhibit six carrier frequencies. One can therefore perform the transformations

$$\begin{aligned} S_{13} =& S_{13}^{(-\omega_p)} e^{-i\omega_p t} + S_{13}^{(+\omega_p)} e^{+i\omega_p t} + S_{13}^{(-\omega_s)} e^{-i\omega_s t} + S_{13}^{(+\omega_s)} e^{+i\omega_s t} \\ &+ S_{13}^{(-\omega_{as})} e^{-i\omega_{as} t} + S_{13}^{(+\omega_{ss})} e^{+i\omega_{ss} t}, \end{aligned} \tag{3.19}$$

$$\begin{aligned} S_{23} =& S_{23}^{(-\omega_s)} e^{-i\omega_s t} + S_{23}^{(+\omega_s)} e^{+i\omega_s t} + S_{23}^{(-\omega_p)} e^{-i\omega_p t} + S_{23}^{(+\omega_p)} e^{+i\omega_p t} \\ &+ S_{23}^{(-\omega_{ss})} e^{-i\omega_{ss} t} + S_{23}^{(+\omega_{as})} e^{+i\omega_{as} t}, \end{aligned} \tag{3.20}$$

where $\omega_{as} \equiv 2\omega_p - \omega_s$ is the anti-Stokes frequency and $\omega_{ss} \equiv 2\omega_s - \omega_p$ is the second Stokes frequency. All the coefficients in Eqs. (3.19) and (3.20) are slowly varying in time. Using the coordinate transformations of this subsection, it is now possible to

generate quantum Langevin equations for the slowly varying system operators.

Field Equations

Using Eqs. (3.11) and (3.18), the Langevin equations for the slowly varying field operators are found to be

$$\dot{a}_p = -\left(\kappa_p + i\Delta_p\right) a_p + g_{p,13} S_{13}^{(-\omega_p)} + g_{p,13}^* \left(S_{13}^{(+\omega_p)}\right)^\dagger + g_{p,23} S_{23}^{(-\omega_p)} + g_{p,23}^* \left(S_{23}^{(+\omega_p)}\right)^\dagger + \sqrt{2\kappa_p}\, a_p^{\text{in}} \tag{3.21}$$

for the pump and

$$\dot{a}_s = -\left(\kappa_s + i\Delta_s\right) a_s + g_{s,13} S_{13}^{(-\omega_s)} + g_{s,13}^* \left(S_{13}^{(+\omega_s)}\right)^\dagger + g_{s,23} S_{23}^{(-\omega_s)} + g_{s,23}^* \left(S_{23}^{(+\omega_s)}\right)^\dagger + \sqrt{2\kappa_s}\, a_s^{\text{in}} \tag{3.22}$$

for the Stokes, where the $\Delta_q \equiv \omega_q^c - \omega_q$ represent the detunings of the driving frequencies from the cold cavity resonances. Note that the primes from Eq. (3.18) have been dropped and it should be understood that a_p and a_s now refer to slowly varying operators. Also note that only the components of S_{13} and S_{23} that produce oscillations near the cavity resonances have been retained. The nonresonant components have been discarded as discussed in the previous subsection. A sample derivation of Eq. (3.21) is provided in Appendix E.

Two-Photon Coherence Equation

The Langevin equation for the 1–2 coherence is obtained in a similar fashion with

the result

$$\begin{aligned}\dot{S}_{12} = &-(\gamma_{21} + i\Delta_{12})S_{12} \\ &+ a_p^\dagger \left[g_{p,23} S_{13}^{(-\omega_{as})} - g_{p,13}^* \left(S_{23}^{(+\omega_{as})} \right)^\dagger \right] - a_p \left[g_{p,23} S_{13}^{(+\omega_s)} - g_{p,13}^* \left(S_{23}^{(-\omega_s)} \right)^\dagger \right] \\ &+ a_s^\dagger \left[g_{s,23} S_{13}^{(-\omega_p)} - g_{s,13}^* \left(S_{23}^{(+\omega_p)} \right)^\dagger \right] - a_s \left[g_{s,23} S_{13}^{(+\omega_{ss})} - g_{s,13}^* \left(S_{23}^{(-\omega_{ss})} \right)^\dagger \right] \\ &+ F_{12}, \end{aligned} \tag{3.23}$$

where $\Delta_{12} \equiv (\omega_2 - \omega_1) - (\omega_p - \omega_s)$ is the two-photon Raman detuning and again, only the near-resonant terms have been included. The nonresonant Fourier components are detuned from the Raman transition by optical frequencies and are therefore neglected. The overall coherence decay constant is defined as

$$\gamma_{21} \equiv \frac{1}{2} \left(\bar{\gamma}_{21} + \tilde{\gamma}_{11} + \tilde{\gamma}_{22} \right), \tag{3.24}$$

and the noise term is

$$\begin{aligned} F_{12} \equiv &+ \sqrt{\bar{\gamma}_{21}} \left(S_{11} - S_{22} \right) B_{12}^{\text{in}} - \sqrt{\bar{\gamma}_{31}} \left(S_{23}^\dagger B_{13}^{\text{in}} \right)^{(-\omega_{21})} - \sqrt{\bar{\gamma}_{32}} \left(B_{23}^\dagger S_{13} \right)^{(-\omega_{21})} \\ &- \sqrt{\tilde{\gamma}_{11}} \left(S_{12} B_{11}^{\text{in}} - B_{11}^{\text{in}\,\dagger} S_{12} \right) + \sqrt{\tilde{\gamma}_{22}} \left(S_{12} B_{22}^{\text{in}} - B_{22}^{\text{in}\,\dagger} S_{12} \right), \end{aligned} \tag{3.25}$$

respectively, where the superscript $(-\omega_{21})$ indicates that only the products that oscillate near the Raman transition frequency are retained.

Single-Photon Coherence Equations

The 1–3 and 2–3 coherences are a bit more complicated. As alluded to earlier in this section, it is not possible to generate slowly varying Langevin equations for the

S_{13} or S_{23} operators themselves. Instead, one can generate slowly varying Langevin equations for the separate Fourier components of the two operators. To see this, one can first use Eq. (3.11) again to generate Langevin equations that are *not* slowly varying for S_{13} and S_{23}. With the use of Eq. (3.18), this yields

$$\begin{aligned}
\dot{S}_{13} = &- \left[\gamma_{31} + i(\omega_3 - \omega_1)\right] S_{13} \\
&- \left[g^*_{p,13}\, a_p (S_{11} - S_{33}) + g^*_{s,23}\, a_s S_{12}\right] \times e^{-i\omega_p t} \\
&+ \left[g^*_{s,13}\, a^\dagger_s (S_{11} - S_{33}) + g^*_{p,23}\, a^\dagger_p S_{12}\right] \times e^{+i\omega_s t} \\
&+ g^*_{p,13}\, a^\dagger_p (S_{11} - S_{33}) \times e^{+i\omega_p t} - g^*_{s,13}\, a_s (S_{11} - S_{33}) \times e^{-i\omega_s t} \\
&- g^*_{p,23}\, a_p S_{12} \times e^{-i(2\omega_p - \omega_s)t} + g^*_{s,23}\, a^\dagger_s S_{12} \times e^{+i(2\omega_s - \omega_p)t} + F_{13},
\end{aligned} \tag{3.26}$$

$$\begin{aligned}
\dot{S}_{23} = &- \left[\gamma_{32} + i(\omega_3 - \omega_2)\right] S_{23} \\
&- \left[g^*_{s,23}\, a_s (S_{22} - S_{33}) + g^*_{p,13}\, a_p S^\dagger_{12}\right] \times e^{-i\omega_s t} \\
&+ \left[g^*_{p,23}\, a^\dagger_p (S_{22} - S_{33}) + g^*_{s,13}\, a^\dagger_s S^\dagger_{12}\right] \times e^{+i\omega_p t} \\
&+ g^*_{s,23}\, a^\dagger_s (S_{22} - S_{33}) \times e^{+i\omega_2 t} - g^*_{p,23}\, a_p (S_{22} - S_{33}) \times e^{-i\omega_p t} \\
&- g^*_{s,13}\, a_s S^\dagger_{12} \times e^{-i(2\omega_s - \omega_p)t} + g^*_{p,13}\, a^\dagger_p S^\dagger_{12} \times e^{+i(2\omega_p - \omega_s)t} + F_{23},
\end{aligned} \tag{3.27}$$

where all the coefficients of the exponentials are slowly varying in time. The primes on the slowly varying field operators have again been dropped. A sample derivation of Eq. (3.26) is provided in Appendix F. The decay constants in these equations are

$$\gamma_{31} \equiv \frac{1}{2}\left(\bar{\gamma}_{31} + \bar{\gamma}_{32} + \tilde{\gamma}_{11} + \tilde{\gamma}_{33}\right), \tag{3.28}$$

and

$$\gamma_{32} \equiv \frac{1}{2}\left(\bar{\gamma}_{32} + \bar{\gamma}_{31} + \bar{\gamma}_{21} + \tilde{\gamma}_{33} + \tilde{\gamma}_{22}\right), \tag{3.29}$$

and the noise terms are

$$\begin{aligned} F_{13} \equiv & \sqrt{\bar{\gamma}_{31}}(S_{11} - S_{33})B_{13}^{\text{in}} + \left(\sqrt{\bar{\gamma}_{32}}S_{12}B_{23}^{\text{in}} - \sqrt{\bar{\gamma}_{21}}S_{23}B_{12}^{\text{in}}\right) \times e^{-i(\omega_p - \omega_s)t} \\ & - \sqrt{\tilde{\gamma}_{11}}(S_{13}B_{11}^{\text{in}} - B_{11}^{\text{in}\,\dagger}S_{13}) + \sqrt{\tilde{\gamma}_{33}}(S_{13}B_{33}^{\text{in}} - B_{33}^{\text{in}\,\dagger}S_{13}), \end{aligned} \tag{3.30}$$

and

$$\begin{aligned} F_{23} \equiv & \sqrt{\bar{\gamma}_{32}}(S_{22} - S_{33})B_{23}^{\text{in}} + \left(\sqrt{\bar{\gamma}_{31}}S_{12}^{\dagger}B_{13}^{\text{in}} + \sqrt{\bar{\gamma}_{21}}B_{12}^{\text{in}\,\dagger}S_{13}\right) \times e^{+i(\omega_p - \omega_s)t} \\ & - \sqrt{\tilde{\gamma}_{22}}(S_{23}B_{22}^{\text{in}} - B_{22}^{\text{in}\,\dagger}S_{23}) + \sqrt{\tilde{\gamma}_{33}}(S_{23}B_{33}^{\text{in}} - B_{33}^{\text{in}\,\dagger}S_{23}). \end{aligned} \tag{3.31}$$

The forms of Eqs. (3.26) and (3.27) make clear the fact that the 1–3 and 2–3 coherences each exhibit Fourier components at six different carrier frequencies. But because none of them are nearly resonant with the atomic transition, one must assume that they all contribute in a non-negligible manner to the coherences. Note the appearance of carrier Fourier components at the anti-Stokes ($\omega_{as} \equiv 2\omega_p - \omega_s$) and second Stokes ($\omega_{ss} \equiv 2\omega_s - \omega_p$) frequencies. Generation of light at the anti-Stokes frequency is addressed in Appendix G.

To generate slowly varying operators for the 1–3 and 2–3 coherences, one can now substitute Eqs. (3.19) and (3.20) into Eqs. (3.26) and (3.27). Because the carrier frequencies differ from one another by optical frequencies, while the coefficients are all slowly varying in time, the terms with different carrier frequencies will not interact.

This can be proven rigorously. Therefore, the terms with like carrier frequencies can be equated to generate six separate slowly varying first-order differential equations; one for each carrier frequency. For the 1–3 coherence, these are given by

$$\dot{S}_{13}^{(-\omega_p)} = -\left[\gamma_{31} + i\Delta\right] S_{13}^{(-\omega_p)} - g_{p,13}^{*}\, a_p (S_{11} - S_{33}) - g_{s,23}^{*}\, a_s S_{12} + F_{13}^{(-\omega_p)}, \tag{3.32a}$$

$$\dot{S}_{13}^{(+\omega_p)} = -\left[\gamma_{31} + i\Delta'_{as}\right] S_{13}^{(+\omega_p)} + g_{p,13}^{*}\, a_p^{\dagger} (S_{11} - S_{33}) + F_{13}^{(+\omega_p)}, \tag{3.32b}$$

$$\dot{S}_{13}^{(-\omega_s)} = -\left[\gamma_{31} + i\Delta_{ss}\right] S_{13}^{(-\omega_s)} - g_{s,13}^{*}\, a_s (S_{11} - S_{33}) + F_{13}^{(-\omega_s)}, \tag{3.32c}$$

$$\dot{S}_{13}^{(+\omega_s)} = -\left[\gamma_{31} + i\Delta'\right] S_{13}^{(+\omega_s)} + g_{s,13}^{*}\, a_s^{\dagger} (S_{11} - S_{33}) + g_{p,23}^{*}\, a_p^{\dagger} S_{12} + F_{13}^{(+\omega_s)}, \tag{3.32d}$$

$$\dot{S}_{13}^{(-\omega_{as})} = -\left[\gamma_{31} + i\Delta_{as}\right] S_{13}^{(-\omega_{as})} - g_{p,23}^{*}\, a_p S_{12} + F_{13}^{(-\omega_{as})}, \tag{3.32e}$$

$$\dot{S}_{13}^{(+\omega_{ss})} = -\left[\gamma_{31} + i\Delta'_{ss}\right] S_{13}^{(+\omega_{ss})} + g_{s,23}^{*}\, a_s^{\dagger} S_{12} + F_{13}^{(+\omega_{ss})}. \tag{3.32f}$$

This last step is only possible because the slowly varying portions corresponding to each carrier frequency do not overlap spectrally. The new slowly varying operators represent separate degrees of freedom (they commute). The detunings in these equations are defined in Table 1 and are shown in Fig. 13.

Table 1. Definitions of single-photon detunings.

Rotating	Counter-Rotating
$\Delta = (\omega_3 - \omega_1) - \omega_p \approx (\omega_3 - \omega_2) - \omega_s$	$\Delta' = (\omega_3 - \omega_1) + \omega_s \approx (\omega_3 - \omega_2) + \omega_p$
$\Delta_{as} = (\omega_3 - \omega_2) - \omega_p$	$\Delta'_{as} = (\omega_3 - \omega_1) + \omega_p$
$\Delta_{ss} = (\omega_3 - \omega_1) - \omega_s$	$\Delta'_{ss} = (\omega_3 - \omega_2) + \omega_s$

The analogous slowly varying equations corresponding to the Fourier components of S_{23} are the same as Eqs. (3.32a) - (3.32f) but with the transformations $p \rightleftharpoons s$, $as \rightleftharpoons ss$ and $1 \rightleftharpoons 2$. The symmetry that allows these transformations is also evident from Fig. 13.

Population Equations

The populations are are also obtained using Eq. (3.11) and are given by

$$\begin{aligned}\dot{S}_{11} =&\bar{\gamma}_{21}S_{22} + \bar{\gamma}_{31}S_{33} + \Big[g_{p,13}\, a_p^\dagger S_{13}^{(-\omega_p)} - g_{p,13}\, a_p S_{13}^{(+\omega_p)} \\ &+ g_{s,13}\, a_s^\dagger S_{13}^{(-\omega_s)} - g_{s,13}\, a_s S_{13}^{(+\omega_s)} + \text{H.c.}\Big] + F_{11}, \qquad (3.33)\\ \dot{S}_{22} =&\bar{\gamma}_{32}S_{33} - \bar{\gamma}_{21}S_{22} + \Big[g_{p,23}\, a_p^\dagger S_{23}^{(-\omega_p)} - g_{p,23}\, a_p S_{23}^{(+\omega_p)} \\ &+ g_{s,23}\, a_s^\dagger S_{23}^{(-\omega_s)} - g_{s,23}\, a_s S_{23}^{(+\omega_s)} + \text{H.c.}\Big] + F_{22}, \qquad (3.34)\\ \dot{S}_{33} =&-\dot{S}_{11} - \dot{S}_{22}, \qquad (3.35)\end{aligned}$$

where atom conservation ($S_{11}+S_{22}+S_{33} = N$) has been used in obtaining Eq. (3.35), and the noise terms are given by

$$F_{11} \equiv -\sqrt{\bar{\gamma}_{21}}\big(S_{12}^\dagger B_{12}^{\text{in}} + B_{12}^{\text{in}\,\dagger} S_{12}\big) - \sqrt{\bar{\gamma}_{31}}\big(S_{13}^\dagger B_{13}^{\text{in}} + B_{13}^{\text{in}\,\dagger} S_{13}\big)^{(\text{dc})}, \qquad (3.36)$$

and

$$F_{22} \equiv -\sqrt{\bar{\gamma}_{32}}\big(S_{23}^\dagger B_{23}^{\text{in}} + B_{23}^{\text{in}\,\dagger} S_{23}\big)^{(\text{dc})} + \sqrt{\bar{\gamma}_{21}}\big(S_{12}^\dagger B_{12}^{\text{in}} + B_{12}^{\text{in}\,\dagger} S_{12}\big), \qquad (3.37)$$

where the superscript (dc) indicates that only the dc Fourier components are retained. The next section is devoted to simplifying the rather unwieldy quantum Langevin equations that were developed in this section.

Simplifications Based on Large Detunings

Up to this point, the large single-photon detunings have only complicated matters by adding additional Fourier components to the single-photon coherences. In this section, the large detunings are used to our advantage by simplifying the quantum Langevin equations. For reference purposes, estimated values of the pertinent rates in this system are provided in Table 2.

Table 2. Parameters used for simplifying the quantum Langevin equations.

Parameter	Symbol	Value
Effective Atom/Field Coupling Constants	$g_{q,ij}/2\pi$	$\sim 10^4 - 10^5$ Hz
Level 2 Population Decay rate	$\bar{\gamma}_{21}/2\pi$	$\sim 10^4 - 10^5$ Hz
Cavity Amplitude Decay Rates	$\kappa_q/2\pi$	$\sim 10^5 - 10^6$ Hz
Level 2 Coherence Decay rate	$\gamma_{21}/2\pi$	$\sim 10^8 - 10^9$ Hz
Level 3 Coherence Decay Rates	$\gamma_{31}/2\pi$, $\gamma_{32}/2\pi$	$\sim 10^9 - 10^{10}$ Hz
Single-Photon Rabi Frequencies	$\Omega_{q,ij}/2\pi$	$\lesssim 10^{10}$ Hz
Single-Photon Detunings	$\Delta/2\pi$	$\sim 10^{15} - 10^{16}$ Hz

The extreme single-photon detunings allow one to make the following simplifications:

(i) Adiabatically eliminate the upper level coherences. As shown by Raymer *et al.* for a single frequency component [77], all of the 1–3 and 2–3 coherence Fourier components can be adiabatically eliminated when the single-photon detunings are much larger than the other rates in the system. One can therefore solve for the

steady-state Fourier components from Eqs. (3.32a)-(3.32f) and their S_{32} counterparts and insert these into the remaining six equations.

(ii) Disregard the single-photon absorption/gain and mode pulling. Terms arise in the two field equations that represent linear absorption/gain (real parts) as well as dispersion (imaginary parts). For near-resonance systems, the real portions can supply the population inversion necessary for laser gain. In the present system, they effectively broaden and pull the frequency of the cavity resonances due to single-photon interactions with the medium. In the limit $\Delta^2\kappa_q \gg \gamma_{ij}|g_{q,ij}|^2$, where the subscript q denotes an optical mode and ij refers to a single-photon transition, the absorption terms can be disregarded. The mode pulling is small and is assumed here to be nullified by active electronic stabilization of the cavity length to the pump laser frequency (i.e. the cavity length is changed to compensate for the refractive index change). It is also assumed that the Stokes field will build on the *active* cavity resonance line-center. Appendix H describes this simplification in more detail.

(iii) Ignore power broadening and AC Stark shifts. Terms arise in the 1–2 coherence equation that are quadratic in the field operators (linear in optical power), and linear in the coherence. In direct analogy with simplification (ii), these terms cause power broadening (real part) and AC Stark shifts (imaginary parts) of the two-photon (1–2) atomic transition. In the limit $\Delta^2\gamma_{21} \gg \gamma_{ij}|\Omega_{q,ij}|^2$, where $\Omega_{q,ij} \equiv g_{q,ij}\, a_q$ is the Rabi frequency for the optical field q driving the ij single-photon atomic transition, the power broadening can be ignored. The AC Stark shift is predicted to be very

mild ($\lesssim 10MHz$) compared to the two-photon resonance width, γ_{21}, for the optical powers considered, and can be compensated easily in practice by tuning the pump laser (with the cavity following). The AC Stark shift is much larger and plays a critical role in electromagnetically induced transparency [78, and references therein]. Appendix I describes this simplification in more detail.

(iv) Neglect spontaneous emission. In the limit of large single-photon detuning relative to the level 3 decay rate, one can make the approximation $(\gamma_{31}+i\Delta)^{-1} \approx (i\Delta)^{-1}$ and likewise for similar terms. As one might expect from the fluctuation/dissipation theorem [73], because the upper level decay can be neglected, it can also be shown that that the associated noise terms entering from the 1–3 and 2–3 coherences are severely diminished by the detuning as well. In the above limits, spontaneous emission will therefore contribute negligibly to the noise of the field and remaining coherence operators, and is neglected (i.e. ignore F_{13} and F_{23}).

With these simplifications, the field and remaining coherence equations become

$$\dot{a}_p = -\kappa_p a_p + i\left(\frac{1}{\Delta}+\frac{1}{\Delta'}\right) g_{p,13}\, g^*_{s,23}\, a_s S_{12} + \sqrt{2\kappa_p}\, a_p^{\text{in}}, \tag{3.38}$$

$$\dot{a}_s = -\kappa_s a_s + i\left(\frac{1}{\Delta}+\frac{1}{\Delta'}\right) g^*_{p,13}\, g_{s,23}\, a_p S_{12}^\dagger + \sqrt{2\kappa_s}\, a_s^{\text{in}}, \tag{3.39}$$

$$\dot{S}_{12} = -(\gamma_{21}+i\Delta_{12})S_{12} + i\left(\frac{1}{\Delta}+\frac{1}{\Delta'}\right) g^*_{p,13}\, g_{s,23}\, (S_{11}-S_{22}) a_p\, a_s^\dagger + F_{12}. \tag{3.40}$$

These equations are significantly more manageable than those of the previous section. In essence, the system initially described by Fig. 13 can now be described by the simpler energy level diagram given in Fig. 14. The large single-photon detunings

have allowed the elimination of all the interactions that are not Raman resonant. Furthermore, the only vestige of *not* invoking the RWA is the Δ' in the gain term of each equation. This extra term can be viewed as the contribution from the counter-rotating version of the Raman process, as can be seen in Fig. 14. Clearly, when the fields are nearly resonant with the single-photon transitions ($\Delta' \gg \Delta$) this contribution becomes negligible. Neglecting the Δ' contribution in this limit is precisely the RWA.

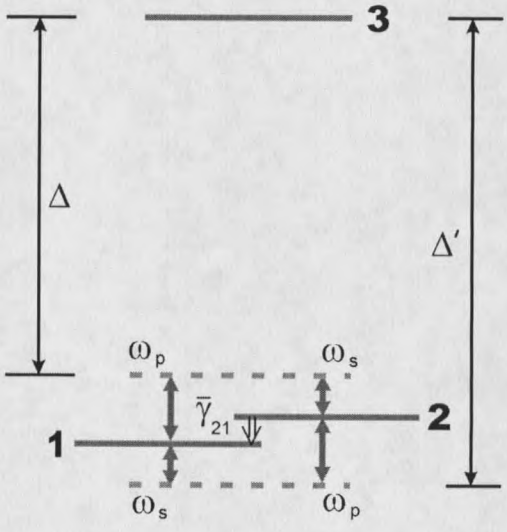

Figure 14. To-scale energy level diagram for the diatomic hydrogen molecule after simplifications based on large single-photon detunings.

Similarly, after adiabatic elimination of the upper level coherences, the populations become

$$\begin{aligned}\dot{S}_{11} =& \bar{\gamma}_{31} S_{33} + \bar{\gamma}_{21} S_{22} \\ &- \left[\frac{1}{\Delta^2} + \frac{1}{(\Delta'_{as})^2}\right] 2\gamma_{31} |g_{p,13}|^2 (S_{11} - S_{33}) |a_p|^2 \\ &- \left[\frac{1}{(\Delta')^2} + \frac{1}{\Delta_{ss}^2}\right] 2\gamma_{31} |g_{s,13}|^2 (S_{11} - S_{33}) |a_s|^2 \\ &+ \left[i \left(\frac{1}{\Delta} + \frac{1}{\Delta'}\right) g_{p,13}\, g^*_{s,23}\, a_p^\dagger\, a_s S_{12} + \text{H.c.}\right] + F_{11}, \end{aligned} \tag{3.41}$$

$$\begin{aligned}\dot{S}_{22} =& \bar{\gamma}_{32} S_{33} - \bar{\gamma}_{21} S_{22} \\ &- \left[\frac{1}{\Delta^2} + \frac{1}{(\Delta'_{ss})^2}\right] 2\gamma_{32} |g_{s,23}|^2 (S_{22} - S_{33}) |a_s|^2 \\ &- \left[\frac{1}{(\Delta')^2} + \frac{1}{(\Delta_{as})^2}\right] 2\gamma_{32} |g_{p,23}|^2 (S_{22} - S_{33}) |a_p|^2 \\ &+ \left[i \left(\frac{1}{\Delta} + \frac{1}{\Delta'}\right) g^*_{p,13}\, g_{s,23}\, a_p\, a_s^\dagger S_{12}^\dagger + \text{H.c.}\right] + F_{22}, \end{aligned} \tag{3.42}$$

$$\dot{S}_{33} = -\dot{S}_{11} - \dot{S}_{22}, \tag{3.43}$$

where the terms arising from single-photon interactions have been retained here so that the populations of the upper level can be estimated later.

Semiclassical Analysis

At this point, one can take the semiclassical limit of the remaining field and atomic equations of motion. This simply entails taking the expectation values of Eqs. (3.38) - (3.43). As noted previously, this eliminates the contributions from the

input operators (except the input pump operator) because the expectation values of their stochastic noise contributions are zero. The following definitions are therefore assigned to distinguish the semiclassical complex variables (c-numbers) from the quantum operators

$$\alpha_q \equiv \langle a_q \rangle, \qquad \alpha_p^{\text{in}} \equiv \sqrt{\tau_{\text{rt}}}\langle a_p^{\text{in}} \rangle, \qquad \text{and} \qquad J_{ij} \equiv \frac{1}{N}\langle S_{ij} \rangle. \tag{3.44}$$

All of the newly assigned variables are unitless. It can be noted here that $|\alpha_p^{\text{in}}|^2$ now represents the unitless semiclassical incident pump power, which is valid for large photon number. Also note that the total population variables have been renormalized to unity so that $J_{11} + J_{22} + J_{33} = 1$.

Furthermore, because the atomic decay rates γ_{21}, $\bar{\gamma}_{31}$, and $\bar{\gamma}_{32}$ are all much larger than the cavity decay rates κ_p and κ_s, one can also adiabatically eliminate the 1–2 coherence and the level 3 population. One can therefore use the steady-state values of these two variables in the remaining four equations of motion.

Simplified Population Equations

Solving for the steady-state 1–2 coherence and plugging it in to the steady state-level 3 population yields

$$J_{33} = \frac{\Gamma_{13}}{(\bar{\gamma}_{31} + \bar{\gamma}_{32})} J_{11} + \frac{\Gamma_{23}}{(\bar{\gamma}_{31} + \bar{\gamma}_{32})} J_{22}, \tag{3.45}$$

where the single-photon absorption (upward transition) rates of population from level

1 to 3 and from level 2 to 3 are defined as

$$\Gamma_{13} \equiv \left[\frac{|\Omega_{p,13}|^2}{\Delta^2} + \frac{|\Omega_{p,13}|^2}{(\Delta'_{as})^2} + \frac{|\Omega_{s,13}|^2}{(\Delta')^2} + \frac{|\Omega_{s,13}|^2}{(\Delta_{ss})^2}\right] 2\gamma_{31}, \tag{3.46}$$

$$\Gamma_{23} \equiv \left[\frac{|\Omega_{s,23}|^2}{\Delta^2} + \frac{|\Omega_{s,23}|^2}{(\Delta'_{ss})^2} + \frac{|\Omega_{p,23}|^2}{(\Delta')^2} + \frac{|\Omega_{p,23}|^2}{(\Delta_{as})^2}\right] 2\gamma_{32}, \tag{3.47}$$

respectively. Because the single-photon detunings (Δ's) are all much larger than any of the Rabi frequencies (Ω's), one can conclude

$$J_{33} \ll 1. \tag{3.48}$$

This simply verifies what may have been suspected from the start; the two-photon Raman process contributes nothing to the upper level population and this population is much less than unity when the single-photon detunings are much greater than the Rabi frequencies.

Similarly, one can define the upward transition rate that is due to the two-photon Raman process as

$$\Gamma_{12} \equiv \left(\frac{2\gamma_{21}}{\gamma_{21}^2 + \Delta_{12}^2}\right)\left(\frac{1}{\Delta} + \frac{1}{\Delta'}\right)^2 |\Omega_{p,13}|^2 |\Omega_{s,23}|^2, \tag{3.49}$$

which has typical value of $\Gamma_{12}/2\pi \lesssim 1$Hz for the fields and detunings of this system. This means that each atom in the beam path is excited by the two-photon process on average less than once per second. The remaining two populations, which are still time dependent, can now be simplified to

$$\dot{J}_{22} = -\bar{\gamma}_{21} J_{22} + \Gamma_{12}, \tag{3.50}$$

$$\dot{J}_{11} = -\dot{J}_{22}, \tag{3.51}$$

where the fact that $\bar{\gamma}_{21} \gg \Gamma_{12}, \Gamma_{23}, \Gamma_{13}$ has been used. These represent simple first order differential equations except for the fact that there is actually field dependence hidden within Γ_{12} in the form of Rabi frequencies. To approximate the behavior of the populations analytically, one can therefore assume that the fields decay rapidly compared to level 2 population. This is typically a very reasonable assumption. In that case, all coefficients are constant and the differential equations can be solved analytically to give

$$J_{22}(t) = \frac{\Gamma_{12}}{\bar{\gamma}_{21}} \left[1 - \exp\left(-\bar{\gamma}_{21} t\right)\right], \tag{3.52}$$

$$J_{11}(t) = 1 - J_{22}(t), \tag{3.53}$$

where it has been assumed that all the population is initially in the ground state. Equation (3.52) is plotted in Fig. 15, where it can be seen that the level two population simply rises monotonically to its steady-state value of $\Gamma_{12}/\bar{\gamma}_{21}$. The time it takes to reach steady state depends only on the level 2 decay rate $\bar{\gamma}_{21}$ for the conditions considered here.

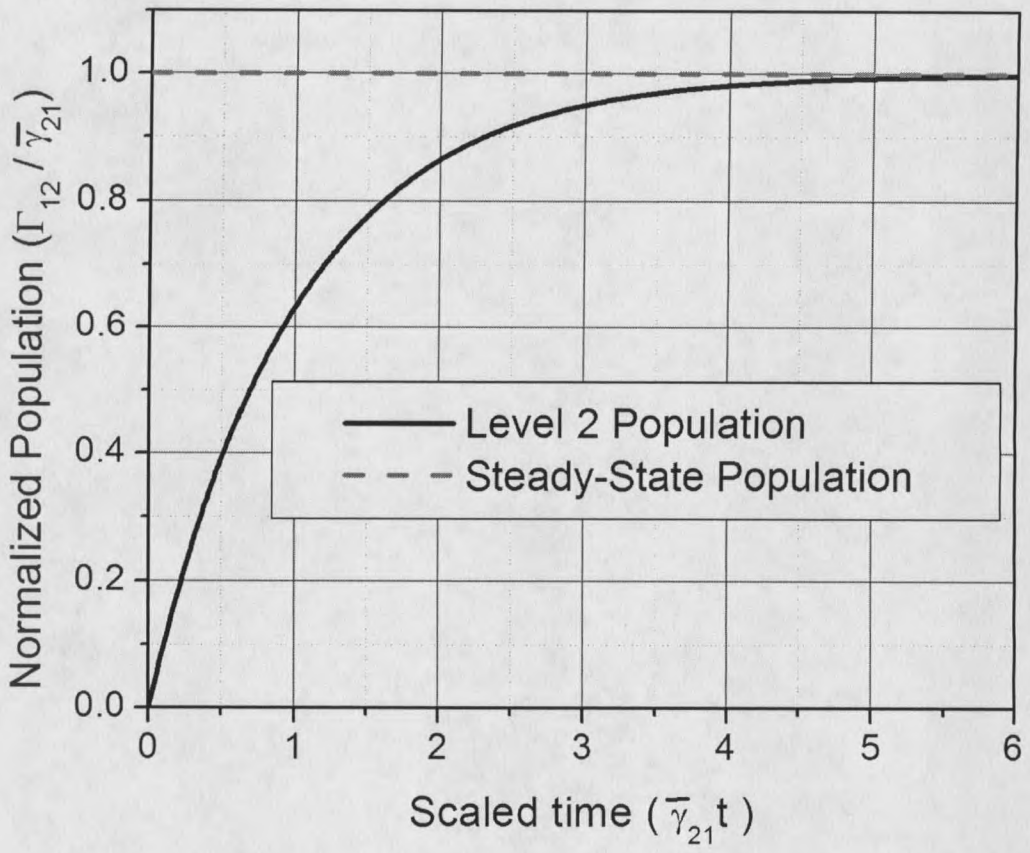

Figure 15. Plot showing the growth of the level two population as a function of the scaled time $\bar{\gamma}_{21}t$, where $\bar{\gamma}_{21}$ is the population decay rate of level two. The population approaches its steady-state value of $\Gamma_{12}/\bar{\gamma}_{21}$ with a rise time of $\bar{\gamma}_{21}^{-1}$, where Γ_{12} is the two-photon excitation rate to level two.

Because the two-photon upward transition rate (Γ_{12}) is much smaller than the level 2 decay rate ($\bar{\gamma}_{21}$), one can conclude that for all times

$$J_{22} \ll 1, \qquad \text{and} \qquad J_{11} \approx 1. \tag{3.54}$$

In other words, one can assume that *all the population remains in the ground state at all times.* This is a critical finding that will simplify future calculations and that will also cause this Raman system to behave like a parametric system.

Simplified Field Equations

Using this knowledge, one can obtain the following simplified Raman field equations

$$\dot{\alpha}_p = -\kappa_p \alpha_p - G_1 |\alpha_s|^2 \alpha_p + \tau_{\rm rt}^{-1} \sqrt{T_{p,0}}\, \alpha_p^{\rm in}, \tag{3.55}$$

$$\dot{\alpha}_s = -\kappa_s \alpha_s + G_1 |\alpha_p|^2 \alpha_s, \tag{3.56}$$

where the Raman gain (rad/s) is defined as

$$G_1 \equiv \left(\frac{\gamma_{21} N}{\gamma_{21}^2 + \Delta_{12}^2}\right) \left(\frac{1}{\Delta} + \frac{1}{\Delta'}\right)^2 |g_{p,13}|^2 |g_{s,23}|^2, \tag{3.57}$$

and dispersion due to the Raman resonance (imaginary contribution to G_1) has been neglected because it is small ($\lesssim$ 1MHz mode pulling relative to a $\sim$ 500MHz Raman linewidth). Note that the field equations decouple from those of the populations because the amount of population in the upper two states is not sufficient to affect the dynamics of the fields.[1] These equations exactly match the forms of Eqns. (B.36) and (B.37) from Appendix B (note, however, that $G_1 \neq G$). This consistency between the classical and quantum mechanical derivations is reassuring. Of course, the steady-state limits of Eqs (3.55) and (3.56) also match the classical results.

Steady-State Behavior

Setting Eqs. (3.55) and (3.56) to zero gives a stable steady-state solution of zero for the (unitless) intracavity Stokes power below threshold. Above threshold, the

[1] Strictly speaking, when thermal effects are included, the fields once again become coupled to the populations.

solutions for the intracavity pump and Stokes unitless powers are

$$|\alpha_p|^2 = \frac{\kappa_s}{G_1}, \tag{3.58}$$

$$|\alpha_s|^2 = \frac{\kappa_p}{G_1}\left(\sqrt{r_p} - 1\right), \tag{3.59}$$

where the cavity field decay rates are given by $\kappa \approx (1 - R_{\rm rt})/2\tau_{\rm rt}$ and the pump rate, defined by the relation

$$r_p \equiv \frac{|\alpha_p^{\rm in}|^2}{|\alpha_p^{\rm th}|^2}, \tag{3.60}$$

is the incident unitless pump power normalized to threshold. The unitless input threshold pump power is given by

$$|\alpha_p^{\rm th}|^2 = \frac{\kappa_p^2 \kappa_s \tau_{rt}^2}{G_1 T_{p,0}}. \tag{3.61}$$

Note that in the process of obtaining these equations from Eqs. (3.55) - (3.56), determination of the Stokes field phase is not permitted. This is a characteristic common to phase insensitive amplification processes and indicates phase diffusion of the Stokes field [79]. Note also that the association of quantities like $|\alpha_p|^2$ with an optical power is a semiclassical approximation that is only strictly valid for photon numbers much greater than one.

The unitless powers from above can be converted to optical powers with standard units [J/s] using the relation

$$P_q = \frac{\hbar\omega_q}{\tau_{\rm rt}}|\alpha_q|^2. \tag{3.62}$$

Equations (3.58) - (3.59) can then be directly compared to Eqs. (2.15) - (2.17) from Chapter 2. This allows one to solve for G_1 in terms of measurable quantities, with the result

$$G_1 = \frac{8\hbar\omega_p\alpha}{\tau_{\rm rt}^2}\frac{\tan^{-1}(L/b)}{\lambda_p + \lambda_s}, \tag{3.63}$$

where α is the plane wave gain coefficient and the fact that $\tau_{\rm rt} = 4L/c$ has been used. By solving Eq. (3.63) for α and using Eq. (3.57), one might be tempted to interpret the resulting relation as a *definition* of α in terms of fundamental parameters of the medium. This would be reasonable if the fields were nearly resonant with the single-photon transitions. For the present far-off-resonance case, however, one must remember that only one upper level (level 3) was considered in this work, whereas all the upper levels (including the continuum) must be included for an accurate estimation of α based on the fundamental parameters of the medium.

Even though the fields no longer depend on the populations, the reverse is definitely not true. The simplified steady-state populations are given by

$$J_{22} = \frac{\Gamma_{12}}{\bar{\gamma}_{21}} \lesssim 10^{-4}, \tag{3.64}$$

$$J_{33} = \frac{\Gamma_{13}}{(\bar{\gamma}_{31} + \bar{\gamma}_{32})} \lesssim 10^{-10}, \tag{3.65}$$

$$J_{11} = 1 - J_{33} - J_{22} \approx 1, \tag{3.66}$$

where the fields are embedded as Rabi frequencies in the Γ's. It should also be noted that the thermal population of level 2 is $\sim 10^{-9}$ for the system at hand. Despite the meager amount of upper state population, the atoms decaying from level 2 can

still dramatically affect the behavior of the fields via heat deposition, as discussed in Chapter 4.

Spatial Considerations

As a side note, the dependence of the gain G_1 from Eq. (3.57) on the spatial characteristics of the pump and Stokes cavity modes can be incorporated by simply defining the number of atoms as that contained in the effective interaction volume of the two cavity modes. That is

$$N \equiv \rho V_{\text{int}}, \tag{3.67}$$

where ρ is the gas density in the Raman cell and the effective volume of the interaction region is given by

$$V_{\text{int}} \equiv \int\int\int_{cavity} |\tilde{u}_p(\mathbf{r})|^2 |\tilde{u}_s(\mathbf{r})|^2 d\mathbf{r}, \tag{3.68}$$

where $\tilde{u}_p(\mathbf{r})$ and $\tilde{u}_s(\mathbf{r})$ are the pump and Stokes spatial modes of the cavity. This is effectively equivalent to including the Boyd-Klienman factor, which was performed in the classical regime for Raman interactions in Ref. [40]. It can be shown rigorously within a quantum mechanical formalism using methods similar to those of Xiao, *et al.* [80].

Connection to the NDOPO

Returning to the fully quantum formalism, but with the knowledge that the vast majority of the population always remains in the ground state, Eqs. (3.38) - (3.40)

can be simplified by setting $S_{11} - S_{22} = N$, where N is the total population in the interaction volume. Furthermore, although it may not seem natural at the moment, one can also make the enlightening variable changes

$$S'_{12} = \frac{S_{12}}{\sqrt{N}} \qquad \text{and} \qquad S^{\text{in}}_{12} \equiv \frac{1}{\sqrt{2\gamma_{21}N}} F_{12}, \tag{3.69}$$

where the noise term F_{12} is given by Eq. (3.25). Substitution of these into Eqs. (3.38) - (3.40) and dropping the prime for notational simplicity yields

$$\dot{a}_p = -\kappa_p a_p + ig\, a_s S_{12} + \sqrt{2\kappa_p}\, a^{\text{in}}_p, \tag{3.70}$$

$$\dot{a}_s = -\kappa_s a_s + ig^*\, a_p S^{\dagger}_{12} + \sqrt{2\kappa_s}\, a^{\text{in}}_s, \tag{3.71}$$

$$\dot{S}_{12} = -(\gamma_{21} + i\Delta_{12}) S_{12} + ig^* a_p\, a^{\dagger}_s + \sqrt{2\gamma_{21}}\, S^{\text{in}}_{12}, \tag{3.72}$$

where

$$g = \sqrt{N}\left(\frac{1}{\Delta} + \frac{1}{\Delta'}\right) g_{p,13}\, g^*_{s,23}. \tag{3.73}$$

A clear symmetry now begins to emerge between Eqs. (3.71) and (3.72). Indeed, the S_{12} operator plays a very similarly to the Stokes field operator in Eqs. (3.70) - (3.72). Moreover, the similarities between S_{12} and an optical mode annihilation operator extend beyond the semiclassical domain as shown in the next subsection.

Operator Correlation Functions

To determine the intensity noise spectra of the emitted light from this system, one must calculate the second order correlation functions of the input operators. For the

field input operators, this is not too tricky, but the coherence input operator requires a bit more thought. Here it is shown that all of the input operators, including $S_{12}^{\rm in}$ exhibit identical second order correlation functions.

The nonvanishing second order correlation functions of the field operators are

$$\langle\, a_p^{\rm in}(t) a_p^{\rm in\,\dagger}(t') \,\rangle = \langle\, a_s^{\rm in}(t) a_s^{\rm in\,\dagger}(t') \,\rangle = \delta(t-t'), \tag{3.74}$$

where the commutation relations from Eq. (3.17) have been used and it has been assumed that the input fluctuations are ordinary vacuum so that $\langle\, a_q^{\rm in\,\dagger} \rightarrow 0$ and $a_q^{\rm in}\rangle \rightarrow 0$.

To calculate the correlation functions for the coherence input operator, one has two choices. First one can continue to use the normal rules of calculus and apply the commutation rules between the system and input operators given in Ref. [52]. For this path, some extra terms show up in the second order correlations that eventually integrate to zero when the noise spectra is calculated. An easier path is to convert to Ito calculus, where the rules of calculus are different, but the system operators commute with the input operators. In this case, no extra terms appear in the second-order correlations. Identical results are obtained using either approach.

Following the latter path, one can verify that the 1–2 input operator is delta correlated $[\langle\, S_{12}^{\rm in}(t) S_{12}^{\rm in\,\dagger}(t') \,\rangle = \delta(t-t')]$ when the input fluctuations are vacuum, just like the field operators. That is, using the commutation relations from Eq. (3.17), the definitions given by Eqs. (3.69) and (3.25), and the fact that the input operators

commute with the system operators for Ito calculus, one can show

$$\langle S_{12}^{\text{in}}(t)S_{12}^{\text{in}}(t')\rangle = \langle S_{12}^{\text{in}\dagger}(t)S_{12}^{\text{in}\dagger}(t')\rangle = 0 \tag{3.75}$$

$$\langle S_{12}^{\text{in}\dagger}(t)S_{12}^{\text{in}}(t')\rangle = \frac{\bar{\gamma}_{32}}{N2\gamma_{21}}\langle S_{33}(t)\rangle\,\delta(t-t') \approx 0 \tag{3.76}$$

$$\begin{aligned}\langle S_{12}^{\text{in}}(t)S_{12}^{\text{in}\dagger}(t')\rangle =& \frac{1}{N2\gamma_{21}}\Big[\bar{\gamma}_{21}\langle S_{11}(t)+S_{33}(t)\rangle + \bar{\gamma}_{31}\langle S_{33}(t)\rangle \\ &+ \tilde{\gamma}_{11}\langle S_{11}(t)\rangle + \tilde{\gamma}_{22}\langle S_{11}(t)\rangle\Big]\delta(t-t') \\ \approx& \frac{1}{2\gamma_{21}}\big(\bar{\gamma}_{21}+\tilde{\gamma}_{11}+\tilde{\gamma}_{22}\big)\delta(t-t') \\ =& \delta(t-t'),\end{aligned} \tag{3.77}$$

just as for the input operator of an optical mode. Note that this is a luxury afforded by the dearth of population in the upper two states.

System Comparison

With the equivalence of the input operator correlation functions established, one can now say that the quantum cw Raman laser equations defined by Eqs. (3.70) - (3.72) are formally identical to those of the nondegenerate optical parametric oscillator (NDOPO) [81] with the following associations: Pump $\leftrightarrow$ Pump, Stokes $\leftrightarrow$ Signal, 1–2 Coherence $\leftrightarrow$ Idler.

The connection between the stimulated Raman and optical parametric processes was actually established from a theoretical standpoint shortly after the discovery of both [82]. At that time, both of the processes were only experimentally achievable in the pulsed regime, making precise experimental comparisons difficult. Since then cw NDOPOs have been experimentally realized and have received a good deal of

theoretical attention [83, and references therein]. But not until recently has the cw Raman process been so isolated from the complicating effects of the single-photon transitions. Indeed, the experimental realization of the far-off-resonance cw Raman laser now allows for detailed comparison with the cw NDOPO and it is fascinating that such a precise correspondence resurfaces after a 35-year hiatus.

The predicted steady-state behaviors of the two systems are identical and have been experimentally verified. They exhibit pump clamping (power limiting) behavior above threshold, which was first identified theoretically for the NDOPO by Siegman [84]. Furthermore, the output modes of both systems exhibit square root dependences on the input pump power, and peak photon conversion efficiencies approaching 100% at four times threshold for single-ended cavities.

All of the population for both systems effectively remains in the ground state. And both systems exhibit phase insensitive amplification when only one output mode is observed. There is actually phase sensitivity hidden between the two output modes for the NDOPO case and between the Stokes and 1–2 coherence for the Raman case. This can be observed by expressing the field operators in terms of amplitude and phase operators (for example $a_s = |a_s| \exp(-i\phi_s)$). It is then straightforward to show from the steady-state solutions of Eq. (3.71) that the following phase relationship holds between the pump, the Stokes (signal) and the 1–2 coherence (idler)

$$\phi_p = \phi_s + \phi_{12} + \pi/2 \tag{3.78}$$

This relation is consistent with the findings of Giordmaine [82] for both the Raman

and NDOPO cases. It is also consistent with other amplification processes for which the driving polarization is 90° out of phase with the amplified light.

Both systems also exhibit the attractive feature of frequency insensitive gain. In other words, the gain doesn't change much if one uses a visible versus a near-infrared pump laser. This is afforded by the large detuning from any single-photon transitions in both the Raman and NDOPO cases and allows for large tuning ranges and spectral coverage of the emitted light.

The only formal difference between these systems lies in what has become the fundamental difference between parametric and stimulated processes [85]. That is, the NDOPO must cope with phase matching difficulties, while the cw Raman laser must deal with challenges associated with heat deposition. There are also differences on a more practical level that can cause their behaviors to deviate from Eqs. (3.70) - (3.72) and from one another. [36, 86]

It is also noted briefly here that there exist less direct connections between the cw Raman laser and the standard (based on population inversion) laser. For instance, when the atomic variables can be eliminated, one can associate the population inversion of the normal laser with the intracavity pump photon number of the NDOPO and Raman systems. Consequently, it is the population inversion that is clamped in the normal laser rather than the intracavity pump power [17, page 514]. Other connections also exist between these systems.

This entire discussion therefore begs the question: "Is the Raman system a laser

or a parametric amplifier?" As unsatisfying as it may be, the answer to this question lies entirely in semantics. Indeed, the word "laser" is a human construction and interestingly, there exist an astounding number of different definitions. Most definitions would probably consider this Raman system a laser, but there is an undeniable link between it and the NDOPO.

Alternative Forms of the Hamiltonian

Due to similarities between the Raman and NDOPO systems, it is natural to think that an alternative form of the Raman Hamiltonian, similar to that of the NDOPO, may be valid. Indeed, such an alternative Hamiltonian does exist and can significantly simplify the quantum mechanical treatment of the cw Raman system. For reference, the original system Hamiltonian from the second section of this chapter is given again here as [see Eqs. (3.2), (3.3), and (3.9)]

$$\begin{aligned} H_{\text{sys}} =& \hbar\omega_1 S_{11} + \hbar\omega_2 S_{22} + \hbar\omega_3 S_{33} + \hbar\omega_p a_p^\dagger a_p + \hbar\omega_s a_s^\dagger a_s \\ &+ i\hbar(a_p^\dagger - a_p)\Big(g_{p,13}\, S_{13} + g_{p,23}\, S_{23} + \text{H.c.}\Big) \\ &+ i\hbar(a_s^\dagger - a_s)\Big(g_{s,13}\, S_{13} + g_{s,23}\, S_{23} + \text{H.c.}\Big). \qquad \text{(Original Form)} \end{aligned} \tag{3.79}$$

Also for reference, the system Hamiltonian for the NDOPO is

$$\begin{aligned} H_{\text{sys}} =& \hbar\omega_p a_p^\dagger a_p + \hbar\omega_s a_s^\dagger a_s + \hbar\omega_i a_i^\dagger a_i \\ &- \hbar\Big(g_{OPO}\, a_p a_s^\dagger a_i^\dagger + \text{H.c.}\Big). \qquad \text{(NDOPO)} \end{aligned} \tag{3.80}$$

One can obtain a simpler Hamiltonian for the Raman system simply by analogy

with that of the NDOPO. Alternatively, Gerry and Eberly [63] utilized the RWA to model two optical modes interacting with a single atom in a Λ configuration, with no decay paths. The optical modes were assumed to be far detuned from the single-photon atomic transitions, but exactly resonant with the two-photon transition. The researchers showed that when the upper level could be adiabatically removed, the single-photon Jaynes-Cummings model for atom-photon interactions [examples of which are shown in Eq. (3.79) without the RWA] could be simplified to a two-photon version. The effective interaction Hamiltonian that they generate is very similar to that of the NDOPO.

I have not assessed the validity of the Gerry and Eberly method. So instead, using the analogy between the far-off-resonance cw Raman system and the NDOPO that was established above, one can obtain the two-photon version of the Raman Hamiltonian

$$\begin{aligned} H_{\text{sys}} =& \hbar\omega_1 S_{11} + \hbar\omega_2 S_{22} + \hbar\omega_p a_p^\dagger a_p + \hbar\omega_s a_s^\dagger a_s \\ & - \hbar\left(g^*\, a_p a_s^\dagger S_{12}^\dagger + \text{H.c.}\right), \qquad \text{(Alternate Form 1)} \end{aligned} \tag{3.81}$$

where g is given by Eq. (3.73). One can quickly verify that applying the Heisenberg equation of motion to this Hamiltonian yields equations that are equivalent to Eqs. (3.38) - (3.40) and therefore averts a good deal of mathematical complexity that was carried out earlier in this chapter. To be clear, the system Hamiltonian given in Eq. (3.81) neglects all single-photon interactions, level 3 population, Stark shifts,

and power broadening. The decay and noise processes associated with level 3 are also implicitly ignored with this system Hamiltonian. It describes only the effects of the two-photon Raman process.

The Hamiltonian given in Eq. (3.81) isn't precisely analogous to that of the NDOPO due to the presence of the level 2 population. However, when the rate of level 2 Raman excitation [see Eq. (3.49)] is small compared to the level 2 decay rate, one can additionally assume that that there is negligible population in level 2. This is the situation that exists for the Raman system that is currently under consideration. Interestingly, in this limit, the 1–2 coherence operator behaves suspiciously like a boson operator (note the commutation relation $[S_{12}, S_{12}^\dagger] = 1$ when $S_{22} \to 0$). The coherence can then be treated in the same manner as a field operator (including reservoir interactions) so that the system Hamiltonian becomes

$$\begin{aligned} H_{\text{sys}} =& \hbar\omega_p a_p^\dagger a_p + \hbar\omega_s a_s^\dagger a_s + \hbar\omega_{21} S_{12}^\dagger S_{12} \\ & - \hbar\left(g^*\, a_p a_s^\dagger S_{12}^\dagger + \text{H.c.}\right). \qquad \text{(Alternate Form 2)} \end{aligned} \tag{3.82}$$

This form of the Raman system Hamiltonian is truly analogous to that of the NDOPO given by Eq. (3.80). It neglects the same processes as the first alternate form, but now none of the free energy of the system resides in the populations. Instead, all of it resides in the fields, as for a parametric process. Here, the coherence "field" operator between the lower two levels can be viewed as the annihilation operator of a molecular vibration or an optical phonon.

It now becomes clear why some authors have successfully applied Hamiltonians similar to Eq. (3.82) but with S_{12} replaced by a phonon operator to Raman systems (see, for instance Ref. [54]). One can now accurately estimate the limits of validity for such an approximate Hamiltonian. Applying the Heisenberg equation of motion to this the second alternate Hamiltonian form yields Eqs. (3.70) - (3.72). As long as one does not need information about the level 2 population (which can be important for thermo-optic considerations), the system Hamiltonian given by Eq. (3.82) accurately describes the behavior of the cw Raman system when the appropriate reservoir interactions are included.

Output Intensity Noise Spectra

he output intensity noise spectra of the generated Stokes light is calculated in this section using the linearization procedure developed by Yamamoto [87] and others [88] and the input/output formalism developed by Collet and Gardiner [89]. The technique has proven to be a valuable tool for analyzing the spectra of parametric systems [81, 90, 91] as well as systems that explicitly involve atomic degrees of freedom [70, 58, 72].

First, the 1–2 coherence can be adiabatically eliminated from Eqs. (3.70) - (3.72) above as for the semiclassical case. However, now quantum noise from the 1–2 coherence finds its way into the remaining two field equations explicitly. Specifically, the

equations become

$$\dot{a}_p = -\kappa_p a_p - G_1\, a_s a_s^\dagger a_p + i\sqrt{2G_1}\, a_s\, S_{12}^{\text{in}} + \sqrt{2\kappa_p}\, a_p^{\text{in}}, \tag{3.83}$$

$$\dot{a}_s = -\kappa_s a_s + G_1 a_p a_p^\dagger a_s + i\sqrt{2G_1}\, a_p \left(S_{12}^{\text{in}}\right)^\dagger + \sqrt{2\kappa_s}\, a_s^{\text{in}}, \tag{3.84}$$

where G_1 is given by Eq. (3.57). These serve as the starting equations for the following derivation of the Stokes laser output intensity noise. They are identical to the semiclassical equations of motion except that the noise contributions are now included.

The procedure is now described. A change of variables is first introduced to decouple the amplitude and phase portions of the field operators. Only the two amplitude equations are of interest for the intensity noise calculation given here. Each amplitude operator is then separated into two portions; the semiclassical mean value, and the small time-dependent fluctuations about this mean value. Such a distinction allows one to linearize the two amplitude equations for small fluctuations about the stable semiclassical mean amplitudes. This linearization dramatically simplifies the subsequent analysis by enabling the use of linear algebra. Accordingly, the equations for the amplitude fluctuations are recast in matrix form and are transformed to the Fourier domain in preparation for an eventual intensity spectra calculation. Using the cavity boundary conditions, the intracavity amplitude fluctuation equations are then transformed to equations for the amplitude fluctuations outside the cavity. From the these fluctuation equations, the intensity noise of the emitted light can be

determined.

Amplitude/Phase Decoupling

As will be shown later, direct detection of a laser's intensity noise only involves the field amplitude; not the phase. It may therefore seem natural to separate the field amplitudes in Eqs. (3.83) and (3.84) from the phases. One can perform the following variable transformation to amplitude and phase operators [87]

$$a_q = \bar{a}_q e^{-i\phi_q}, \qquad \text{for } q = p, s \tag{3.85}$$

and similarly for all the input operators, where

$$\bar{a}_q \equiv \sqrt{a_q a_q^\dagger} \qquad \text{and} \qquad \phi_q \equiv \frac{i}{2} \ln\left(\frac{a_q}{a_q^\dagger}\right). \tag{3.86}$$

The transformation given above is only valid when the photon number is much larger than unity [87, and references therein]. This condition is easily satisfied for the system at hand. It should also be noted here that a field quadrature expansion yields identical results to this amplitude/phase expansion [81]. Inserting the transformations given by Eq. (3.85) into Eqs. (3.83) and (3.84) produces the following two amplitude equations

$$\begin{aligned}\frac{d}{dt}\bar{a}_p =& -\kappa_p \bar{a}_p - G_1 \bar{a}_s^2 \bar{a}_p \\ &+ i\sqrt{2G}\,\bar{a}_s\,\bar{S}_{12}^{\text{in}} e^{-i(\phi_s+\phi_{12}-\phi_p)} + \sqrt{2\kappa_p}\,\bar{a}_p^{\text{in}},\end{aligned} \tag{3.87}$$

$$\begin{aligned}\frac{d}{dt}\bar{a}_s =& -\kappa_s \bar{a}_s + G_1 \bar{a}_p^2 \bar{a}_s \\ &+ i\sqrt{2G}\,\bar{a}_p\,\bar{S}_{12}^{\text{in}} e^{-i(\phi_p-\phi_{12}-\phi_s)} + \sqrt{2\kappa_s}\,\bar{a}_s^{\text{in}}.\end{aligned} \tag{3.88}$$

Using the phase relationship between the fields given by Eq. (3.78), the amplitude operators completely decouple from the phase operators. This is quite expected for phase insensitive amplification processes like Raman lasing. Because only the amplitude equations are of interest for the intensity noise, this decoupling therefore conveniently reduces the number of pertinent equations from four (a_p, $a_p^\dagger$, a_s, and $a_s^\dagger$) to two ($\bar{a}_p$ and $\bar{a}_s$).

Linearization

The two remaining equations are still nonlinear, thereby prohibiting straightforward analytical solutions. To alleviate this difficulty, one can first make an explicit distinction between the semiclassical steady-state field amplitude, and the small amplitude fluctuations about this mean value as is often done (see, for instance Ref. [92, page 34]). Accordingly, the following field fluctuation *operator* is defined

$$\delta\bar{a}_q(t) = 2\left(\bar{a}_q(t) - |\alpha_q|\right), \tag{3.89}$$

so that

$$\bar{a}_q(t) = |\alpha_q| + \frac{1}{2}\delta\bar{a}_q(t), \tag{3.90}$$

where the factor of two is included for later mathematical convenience. Now all the time dependence (and all the quantum nature) of each field amplitude is contained within the fluctuation operator $\delta\bar{a}_q(t)$, while $|\alpha_q|$ represents the real-valued steady-state semiclassical field amplitude, which is independent of time. The input

fluctuation operators are represented in a similar manner. However, only the input pump operator will have a nonzero mean deterministic value. The other two input operators represent purely stochastic noise and fluctuate about zero mean values (it is assumed that there is no Stokes seed).

These newly-defined field and input fluctuation operators can be inserted into Eqs. (3.87) and (3.88). Doing this generates both the behavior of the semiclassical steady-state amplitudes as well as that of the amplitude fluctuations. For the steady-state behavior above threshold, one recovers the previous semiclassical results (Eqs. 3.58 and 3.59), which are written here as

$$|\alpha_p| = \sqrt{\frac{\kappa_s}{G_1}}, \qquad \text{and} \qquad |\alpha_s| = \sqrt{\frac{s\,\kappa_p}{G_1}}, \tag{3.91}$$

with

$$s \equiv \sqrt{r_p} - 1, \tag{3.92}$$

where the pump rate r_p is defined in Eq. (3.60). And for the time-dependent amplitude fluctuation operators, one obtains the two linear equations

$$\begin{aligned} \frac{d}{dt}\delta\bar{a}_p = &- \left(\kappa_p + G_1|\alpha_s|^2\right)\delta\bar{a}_p - 2G|\alpha_p||\alpha_s|\,\delta\bar{a}_s \\ &- \sqrt{2G}\,\delta\bar{S}_{12}^{\text{in}} + \sqrt{2\kappa_p}\,\delta\bar{a}_p^{\text{in}}, \end{aligned} \tag{3.93}$$

$$\begin{aligned} \frac{d}{dt}\delta\bar{a}_s = &- \left(\kappa_s - G_1|\alpha_p|^2\right)\delta\bar{a}_s + 2G|\alpha_p||\alpha_s|\,\delta\bar{a}_p \\ &+ \sqrt{2G}\,\delta\bar{S}_{12}^{\text{in}} + \sqrt{2\kappa_s}\,\delta\bar{a}_s^{\text{in}}, \end{aligned} \tag{3.94}$$

where it is understood that all the fluctuation operators are functions of time. In obtaining these fluctuation equations it has been assumed that the steady-state field

amplitudes are very large compared to the associated fluctuations ($|\alpha_q| \gg |\delta a_q(t)|$) so that second order fluctuation terms can be neglected. In practice, this linear approximation is incredibly good.

The fact that the above amplitude fluctuation equations are now linear significantly simplifies subsequent analysis by enabling the use of linear algebra. Specifically, Eqs. (3.93) and (3.94) can be written in the compact form

$$\frac{d}{dt}\,\delta\mathbf{a}(t) = -\underline{\mathbf{A}}\,\delta\mathbf{a}(t) + \underline{\mathbf{B}}\,\delta\mathbf{S}^{\text{in}}(t) + \underline{\mathbf{C}}\,\delta\mathbf{a}^{\text{in}}(t), \tag{3.95}$$

where the following vectors and matrices have been defined

$$\delta\mathbf{a} = \begin{pmatrix} \delta\bar{a}_p \\ \delta\bar{a}_s \end{pmatrix}, \qquad \delta\mathbf{S}^{\text{in}} = \delta\bar{S}_{12}^{\text{in}} \begin{pmatrix} 1 \\ 1 \end{pmatrix}, \qquad \delta\mathbf{a}^{\text{in}} = \begin{pmatrix} \delta\bar{a}_p^{\text{in}} \\ \delta\bar{a}_s^{\text{in}} \end{pmatrix}, \tag{3.96}$$

$$\underline{\mathbf{A}} = \begin{pmatrix} \kappa_p + G_1|\alpha_s|^2 & 2G_1|\alpha_p||\alpha_s| \\ -2G_1|\alpha_p||\alpha_s| & \kappa_s - G_1|\alpha_p|^2 \end{pmatrix} = \begin{pmatrix} (1+s)\kappa_p & 2\sqrt{s\,\kappa_p\kappa_s} \\ -2\sqrt{s\,\kappa_p\kappa_s} & 0 \end{pmatrix}, \tag{3.97}$$

$$\underline{\mathbf{B}} = \begin{pmatrix} -\sqrt{2G_1}|\alpha_s| & 0 \\ 0 & \sqrt{2G_1}|\alpha_p| \end{pmatrix} = \begin{pmatrix} -\sqrt{2s\,\kappa_p} & 0 \\ 0 & \sqrt{2\,\kappa_p} \end{pmatrix}, \tag{3.98}$$

$$\underline{\mathbf{C}} = \text{diag}\left(\sqrt{2\kappa_p}, \sqrt{2\kappa_s}\right). \tag{3.99}$$

Note that the relations given by Eqs. (3.91) and (3.92) have been used.

Input/Output Formalism

The previous analysis has generated a set of linear equations describing the amplitude fluctuations in time for the fields within the cavity. However, the noise spectra in the Fourier domain for the field fluctuations outside the cavity are sought. One can

therefore next take the Fourier transform of Eq. (3.95) and solve for the intracavity field fluctuations (in the frequency domain) to give

$$\delta\tilde{\mathbf{a}}(\omega) = (i\omega + \underline{\mathbf{A}})^{-1}\left[\underline{\mathbf{B}}\,\delta\tilde{\mathbf{S}}^{\mathrm{in}}(\omega) + \underline{\mathbf{C}}\,\delta\tilde{\mathbf{a}}^{\mathrm{in}}(\omega)\right], \tag{3.100}$$

where the fact has been used that the Fourier transform of the derivative of an operator can be expressed by multiplying the transform of the operator by $i\omega$. The operators in Fourier space are denoted with tilde's and are defined by

$$\delta\tilde{\mathbf{a}}(\omega) = \frac{1}{\sqrt{2\pi}}\int_{-\infty}^{\infty} dt\,\delta\mathbf{a}(t)e^{i\omega t}, \tag{3.101}$$

and similarly for the input operators.

One can now use the cavity boundary conditions [52]

$$\delta\tilde{\mathbf{a}}^{\mathrm{out}}(\omega) = \underline{\mathbf{C}}\,\delta\tilde{\mathbf{a}}(\omega) - \delta\tilde{\mathbf{a}}^{\mathrm{in}}(\omega), \tag{3.102}$$

to find the output amplitude fluctuations as functions of the input amplitude fluctuations. The vector $\delta\mathbf{a}^{\mathrm{out}}$ is defined analogously to its input counterpart. Inserting Eq. (3.100) into Eq. (3.102) yields

$$\delta\tilde{\mathbf{a}}^{\mathrm{out}}(\omega) = \underline{\mathbf{C}}\,(i\omega + \underline{\mathbf{A}})^{-1}\,\underline{\mathbf{B}}\,\delta\tilde{\mathbf{S}}^{\mathrm{in}}(\omega) + \left[\underline{\mathbf{C}}\,(i\omega + \underline{\mathbf{A}})^{-1}\,\underline{\mathbf{C}} - \underline{\mathbf{1}}\right]\delta\tilde{\mathbf{a}}^{\mathrm{in}}(\omega), \tag{3.103}$$

where $\underline{\mathbf{1}}$ is the identity matrix. One can now relate these output amplitude fluctuations to the measured intensity noise of the laser.

Intensity Noise

One can define a (unitless) output intensity operator for the field through

$$I_q^{\mathrm{out}} = a_q^{\mathrm{out}} a_q^{\dagger\,\mathrm{out}}. \qquad \text{for } q = p, s \tag{3.104}$$

The expectation value of this operator gives the mean photon flux (photons/second) exiting the cavity when the photon number is much larger than one. Like the input operators, the output field operators are defined with units $\sqrt{Hz}$. Inserting the expression for the field operator given by Eq. (3.85), and using the fluctuation operator definition given by Eq. (3.90) this equation becomes

$$\begin{aligned} I_q^{\text{out}}(t) &= \left[\bar{a}_q^{\text{out}}(t)^2\right] \\ &= \left[|\alpha_q^{\text{out}}| + \frac{1}{2}\,\delta\bar{a}_q^{\text{out}}(t)\right]^2 \\ &\approx |\alpha_q^{\text{out}}|^2 + |\alpha_q^{\text{out}}|\,\delta\bar{a}_q^{\text{out}}(t), \end{aligned} \tag{3.105}$$

where the second order fluctuations have again been neglected in the last step. This relation shows that direct detection of a laser's intensity noise is proportional to the fluctuations in the field amplitude, and has nothing to do with the field phase. One can now define the fluctuation operator for the intensity as

$$\delta I_q^{\text{out}}(t) = |\alpha_q^{\text{out}}|\,\delta\bar{a}_q^{\text{out}}(t), \tag{3.106}$$

In practice, the intensity noise spectra of the laser output is obtained using a power spectrum analyzer which measures the power spectral density as a function of rf

frequency. Mathematically, this measurement is described by

$$\begin{aligned} S_q^{\text{out}}(\omega) &= \int_{-\infty}^{\infty} \langle\, \delta I_q^{\text{out}}(t+\tau)\delta I_q^{\text{out}}(t)\,\rangle e^{-i\omega\tau} d\tau \\ &= |\alpha_q^{\text{out}}|^2 \int_{-\infty}^{\infty} \langle\, \delta\bar{a}_q^{\text{out}}(t+\tau)\;\delta\bar{a}_q^{\text{out}}(t)\,\rangle e^{-i\omega\tau} d\tau \\ &= |\alpha_q^{\text{out}}|^2 \langle\, \delta\tilde{a}_q^{\text{out}}(\omega)\;\left(\delta\tilde{a}_q^{\text{out}}(\omega)\right)^{\dagger}\rangle \\ &= |\alpha_q^{\text{out}}|^2 \,\langle\, |\delta\tilde{a}_q^{\text{out}}(\omega)|^2\,\rangle, \end{aligned} \tag{3.107}$$

where the Wiener-Khintchin theorem has been used to get from the second to the third step [81]. This valuable result shows that the output intensity noise is simply related to the variance of the amplitude operator.

The noise spectra are often normalized to that of a coherent state light source of the same average power. This universal noise reference is called the standard quantum limit (SQL) and is often referred to as shot noise. Many sources of light can closely approximate a coherent state, making this an incredibly useful normalization from an experimental standpoint.

To normalize Eq. (3.107) to the SQL, it can be divided by a power spectral density of the same average intensity, but with the output fluctuation operators replaced by vacuum field fluctuation operators (i.e. a coherent state). As shown in Appendix J, the power spectral density for a coherent state is simply $S_q^{\text{coh}}(\omega) = |\alpha_q^{\text{out}}|^2$. Using the symbol $V_q^{\text{out}}(\omega)$ to represent the power spectral density normalized to the SQL, one obtains

$$V_q^{\text{out}}(\omega) \equiv \frac{S_q^{\text{out}}(\omega)}{S_q^{\text{coh}}(\omega)} = \langle\, |\delta\tilde{a}_q^{\text{out}}(\omega)|^2\,\rangle. \tag{3.108}$$

One can now use Eq. (3.109) to obtain the output intensity noise as a function of the input intensity noise. Specifically, the matrix defined by the vector product

$$\begin{aligned}\underline{\mathbf{V}}^{\text{out}}(\omega) &= \langle \delta\tilde{\mathbf{a}}^{\text{out}}(\omega) \left(\delta\tilde{\mathbf{a}}^{\text{out}}(\omega)\right)^{\dagger} \rangle \\ &= \begin{pmatrix} \langle\, |\delta\tilde{a}_p^{\text{out}}(\omega)|^2 \,\rangle & \langle\, \delta\tilde{a}_p^{\text{out}}(\omega) \left(\delta\tilde{a}_s^{\text{out}}(\omega)\right)^{\dagger} \,\rangle \\ \langle\, \delta\tilde{a}_s^{\text{out}}(\omega) \left(\delta\tilde{a}_p^{\text{out}}(\omega)\right)^{\dagger} \,\rangle & \langle\, |\delta\tilde{a}_s^{\text{out}}(\omega)|^2 \,\rangle \end{pmatrix}, \end{aligned} \tag{3.109}$$

exhibits the desired quantity in the bottom right diagonal element, $V_{22}^{\text{out}}(\omega)$. It should be noted that a dagger superscript of a vector quantity represents the conjugate transpose of that vector. Using a computer to calculate the elements of $V_{22}^{\text{out}}(\omega)$ analytically yields

$$\begin{aligned} V_s^{\text{out}}(\omega) =& V_{22}^{\text{out}}(\omega) \\ =& \frac{4\kappa_s^2 \left[\omega^2 + \kappa_p^2(s-1)^2\right]}{\left(\omega^2 - 4\kappa_p\kappa_s s\right)^2 + \kappa_p^2(s+1)^2\omega^2} \times V_{\text{atoms}}^{\text{in}}(\omega) \\ &+ \frac{16\kappa_p^2\kappa_s^2 s}{\left(\omega^2 - 4\kappa_p\kappa_s s\right)^2 + \kappa_p^2(s+1)^2\omega^2} \times V_p^{\text{in}}(\omega) \\ &+ \frac{\omega^4 + \left[\kappa_p^2(1+s)^2 + 4\kappa_s^2 - 8\kappa_p\kappa_s s\right]\omega^2 + 4\kappa_p^2\kappa_s^2(s-1)^2}{\left(\omega^2 - 4\kappa_p\kappa_s s\right)^2 + \kappa_p^2(s+1)^2\omega^2} \times V_s^{\text{in}}(\omega), \end{aligned} \tag{3.110}$$

where the input variances are defined as

$$V_{\text{atoms}}^{\text{in}}(\omega) = \langle\, |\delta\tilde{S}_{12}^{\text{in}}(\omega)|^2 \,\rangle, \tag{3.111}$$

$$V_p^{\text{in}}(\omega) = \langle\, |\delta\tilde{a}_p^{\text{in}}(\omega)|^2 \,\rangle \tag{3.112}$$

$$V_s^{\text{in}}(\omega) = \langle\, |\delta\tilde{a}_s^{\text{in}}(\omega)|^2 \,\rangle \tag{3.113}$$

The first term on the right side of Eq. (3.110) represents the noise contribution from

the atoms while the second and third terms are the contributions from pump and Stokes input fields, respectively.

Taking the input variances of the atoms and the Stokes field to be ordinary vacuum ($V_{\text{atoms}}^{\text{in}}(\omega) = V_s^{\text{in}}(\omega) = 1$), but leaving the input pump variance as a variable parameter gives the following analytical result for the the output Stokes intensity noise

$$V_s^{\text{out}}(\omega) = \frac{\omega^4 + \left[\kappa_p^2(1+s)^2 + 8\kappa_s^2 - 8\kappa_p\kappa_s s\right]\omega^2 + 8\kappa_p^2\kappa_s^2\left[(s-1)^2 + 2sV_p^{\text{in}}(\omega)\right]}{\left(\omega^2 - 4\kappa_p\kappa_s s\right)^2 + \kappa_p^2(s+1)^2\omega^2}, \tag{3.114}$$

This analytical solution for the Stokes laser intensity noise spectra is the primary result of this section. An analogous result for the emitted pump light intensity noise can be calculated in the same manner. Furthermore, using the formalism of this section, one can also calculate the intensity correlations between the output pump and Stokes. A thorough analysis of the Stokes intensity noise is given in the next subsection.

Stokes Intensity Noise Analysis

Although it may seem difficult to extract much insight from Eq. (3.114), several limiting cases can shed some light on the underlying physics involved. In particular, one can analyze the Stokes intensity noise behavior as a function of pump rate for very low and very high Fourier frequencies. Figure 16 illustrates the pump rate behavior of the intensity noise for Fourier frequencies below the cavity linewidths ($\omega \ll \kappa_p, \kappa_s$) and for several different input pump noise levels. A coherent state input pump noise

corresponds to $V_p^{\text{in}}(\omega) = 1$. The behavior is plotted on both linear [Fig. 16(a)] and a log-log [Fig. 16(b)] scales. Also, Eq. (3.114) becomes

$$V_s^{\text{out}}(\omega) = \frac{\left[(s-1)^2 + 2sV_p^{\text{in}}(\omega)\right]}{2s^2} \qquad (\omega \ll \kappa_p, \kappa_s) \qquad (3.115)$$

in the limit of low Fourier frequency. From the figures and from Eq. (3.115), first note that the Stokes intensity noise is well above the SQL near threshold ($s \approx 0$, $r_p \approx 1$) for all curves. This system is therefore inherently noisy near threshold, a trait that is shared with other laser systems. However, it is very important to note that the output Stokes intensity noise is equal to the input pump noise [$V_s^{\text{out}}(\omega) = V_p^{\text{in}}(\omega)$] at four times threshold ($s = 1$, $r_p = 4$) for all curves. Vertical lines at $r_p = 4$ have been provided on both plots to emphasize this point. This feature can be confirmed using Eq. (3.115) with $s = 1$. The system therefore displays *perfect photon statistics transfer from the input pump to the output Stokes for a pump rate of four times threshold and frequencies below the cavity linewidths.* This is also consistent with the steady-state results of Chapter 2 indicating a photon conversion efficiency of 100% occurring at $r_p = 4$.

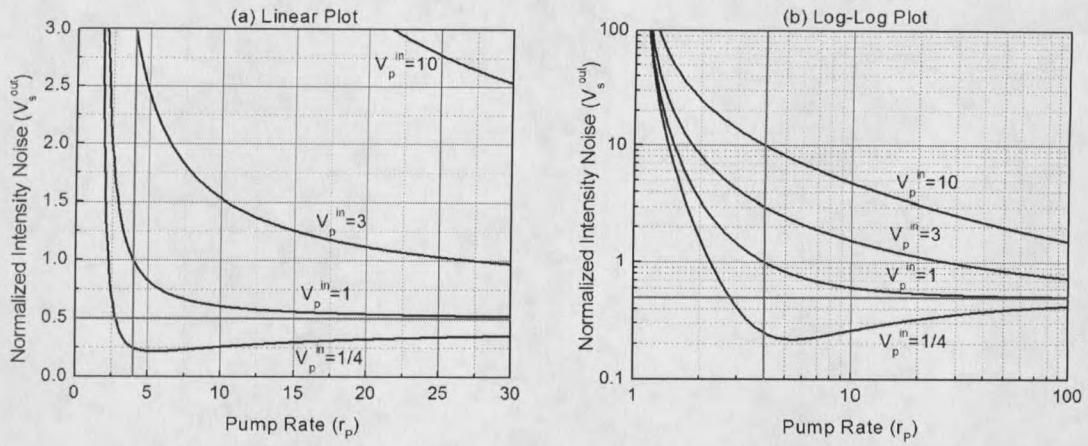

Figure 16. (a) Linear and (b) log-log plots of the Stokes intensity noise relative to the SQL as a function of pump rate for frequencies well below the cavity linewidths. Curves for several different values of the input pump intensity noise $[V_p^{\rm in}(\omega)]$ are shown. The system exhibits perfect photon statistics transfer from pump to Stokes at four times threshold and the intensity noise approaches 50% below the SQL in the limit of large pump rate.

It is also interesting to note that the output intensity noise can drop below the shot noise level $[V_s^{\rm out}(\omega) = 1]$ for higher pump rates and asymptotically approaches $V_s^{\rm out}(\omega) = 1/2$ in the limit of large pump rate ($r_p \gg 1$) even when the input pump noise is greater than vacuum. This feature is observed most easily in the log-log plot and can also be confirmed by simply taking the limit $s \to \infty$ in Eq. (3.115). This system is therefore predicted to approach *50% intensity noise reduction below the SQL for frequencies within both of the cavity bandwidths and for high pump rates.*

Up to now, only the low frequency limit of Eq. (3.114) has been considered. On the other hand, for frequencies much larger than the cavity bandwidths, the intensity noise approaches the SQL for all pump rates and for all input pump noise levels. This simply expresses the fact that the cavity acts as a low-pass filter and that the only

contribution to the output Stokes intensity noise far above the cavity bandwidths is the reflected vacuum noise. This can be confirmed by taking the limit $\omega \rightarrow \infty$ in Eq. (3.114). Using Eq. (3.110), it is also possible to determine the particular contributions to the total intensity noise from each of the three noise sources (input pump noise, input Stokes noise, and input coherence noise).

Although the low and high frequency limits are simpler from a mathematical standpoint, much of the interesting behavior can occur for frequencies between the extremely low and extremely high limits. This behavior depends critically on the ratio of the two cavity decay rates. Figures 17 and 18 help to illustrate the issues involved.

Figure 17(a) shows the Stokes intensity noise as a function of Fourier frequency for a pump rate of four times threshold ($s = 1$, $r_p = 4$) and an input pump noise 10 times greater than shot noise [$V_p^{\text{in}}(\omega) = 10$]. The Fourier frequency on the horizontal axis is given relative to $sqrt(\kappa_p \kappa_s)$ so that the curves can be compared on even ground. In the figure several curves are given corresponding to several different values of the cavity decay rate ratio (κ_s/κ_p). As this ratio increases, relaxation oscillations become undamped as evidenced by the increasing noise peak. In general, *decreasing the cavity decay rate ratio (i.e. making the Stokes cavity finesse greater than that of the pump) suppresses relaxation oscillations.* This is consistent with previous findings in the time domain [69].